On Intermediate Models for Barotropic Continental Shelf and Slope Flow Fields. Part III: Comparison of Numerical Model Solutions in Periodic Channels

J. S. ALLEN, J. A. BARTH AND P. A. NEWBERGER

College of Oceanography, Oregon State University, Corvallis, Oregon

(Manuscript received 15 February 1990, in final form 2 July 1990)

ABSTRACT

The study of intermediate models for barotropic continental shelf and slope flow fields initiated in Parts I and II is continued. The objective is to investigate the possible use of intermediate models for process and data assimilation studies of nonlinear mesoscale eddy and jet current fields over the continental shelf and slope. Intermediate models contain physics between that in the primitive equations and that in the quasi-geostrophic equations and are capable of representing subinertial frequency motion over the O(1) topographic variations typical of the continental slope while filtering out high-frequency gravity–inertial waves. We concentrate on the application of intermediate models to the *f*-plane shallow-water equations. The accuracy of several intermediate models is evaluated here by a comparison of numerical finite-difference solutions with those of the primitive shallow-water equations (SWE) and with those of the quasi-geostrophic equations (QG) for flow in a periodic channel. The intermediate models that we consider are based on the balance equations (BE), the balance equations derived from momentum equations (BEM), the potential vorticity conserving linear balance equations (LQBE), the hybrid balance equations (HBE), the near balance equation (NBE), a geostrophic vorticity (GV) approximation, the geostrophic momentum (GM) approximation, and the quasi-geostrophic momentum and full continuity equations (IM). The periodic channel provides a basic geometry for the study of physical flow processes over the continental shelf and slope. Wall boundary conditions are formulated for the intermediate models and implemented in the numerical finite-difference approximations. The ability of intermediate models to represent linear ageostrophic coastally trapped waves, i.e., Kelvin and continental shelf waves, is verified by numerical experiments. The results of numerical solution intercomparisons for initial-value problems involving O(1) topographic variations are as follows. For flow at small local Rossby number $|\epsilon_L| < 0.2$, where ϵ_L is given by the magnitude of the vorticity divided by f, all of the intermediate models do well, while the QG model does poorly. For flows with larger values of $|\epsilon_L|$, e.g., $|\epsilon_L| \approx 0.5$, the performance of the different intermediate models varies. BEM and BE consistently give extremely accurate solutions while the solutions from LQBE are almost as good. The other models are substantially less accurate with errors generally increasing in the order NBE, HBE, GV, GM, IM. The QG solution always has the largest errors. Consistent with the results from the studies in Part II in a doubly periodic domain, the balance equations BE and BEM, followed closely by LQBE, appear to be the most accurate intermediate models.

1. Introduction

We continue the study of intermediate models initiated in Part I (Allen et al. 1990) and Part II (Barth et al. 1990). Our objective is to assess the possibility of the use of intermediate models for the study of nonlinear, mesoscale physical oceanographic processes over the continental shelf and slope. Intermediate models (McWilliams and Gent 1980) contain physics between that in the full primitive equations and that in the quasi-geostrophic approximation. They are capable of representing flows over O(1) topographic variations, with accompanying O(1) variations in height of the density surfaces, for which the quasi-geostrophic approximation is not formally valid. In addition, intermediate models systematically filter out the high-frequency gravity-inertial waves present in the primitive equations. This may lead to simplifications, relative to the primitive equations, in the application of intermediate models to data assimilation studies. Examples of some of the more widely known intermediate models are the balance equations (Charney 1955; Bolin 1955; Lorenz 1960; Gent and McWilliams 1983a) and the geostrophic momentum approximation (Hoskins 1975). The latter is frequently employed in conjunction with a transformation to geostrophic coordinates after which the model is referred to as the semi-geostrophic equations.

Based on the considerable success of the quasi-geostrophic (QG) equations as an approximate model for mesoscale atmospheric and oceanic motion (Pedlosky 1987), it seems natural to consider the possibility that some appropriate approximate form of the primitive equations might be applicable to mesoscale flow fields over the continental slope where QG is not valid. We have in mind an approximation similar to QG that

Corresponding author address: Dr. John S. Allen, College of Oceanography, Oregon State University, Oceanography Admin Bldg 104, Corvallis, OR 97331-5503.

would be based on the assumption of a small Rossby number and would filter out high-frequency gravity–inertial waves, but that would extend the range of validity of QG to regions with O(1) bottom topographic variations. It seems to us that such a model would be potentially of great use for the study of mesoscale physical oceanographic processes in coastal seas.

We have pursued the above objective by proceeding with a set of comparative studies of intermediate models for rotating fluid flows over topography. We concentrate in these initial studies on motion governed by the *f*-plane shallow-water equations (SWE). In Part I, we discussed the formulation for the SWE of all of the previously developed intermediate models known to us and we presented some new, as well as some modified, models. The ability of intermediate models to represent linear ageostrophic coastally trapped Kelvin and continental shelf waves was demonstrated analytically. Model accuracy as a function of Rossby number was examined by a comparison of exact nonlinear solutions that exist for the SWE (Ball 1965; Cushman-Roisin et al. 1985) with corresponding analytical solutions of the intermediate models. In addition, the model equations were written in a form appropriate for numerical solution in physical coordinates and a common method of formulation was given for all of the different intermediate models.

In Part II, we continued the assessment of intermediate model accuracy by the comparison of numerical finite-difference solutions of the SWE, QG and twelve different intermediate models for initial-value problems involving flow over O(1) topographic variations. A doubly periodic domain was utilized there because the methods of application of wall boundary conditions for some intermediate models are not straightforward and require testing in their own right. The formulation of initial-value problems in doubly periodic domains allowed the model solutions to evolve strictly according to internal model dynamics isolated from any effects of wall boundary conditions. The results clearly indicated that balance-equation–type intermediate models give the most accurate solutions.

In the present study, we continue the evaluation of intermediate models through comparison of numerical finite-difference solutions to initial-value problems in a periodic channel. This naturally involves the formulation and implementation of wall boundary conditions. The periodic channel geometry allows the testing of the ability of the intermediate models, and of their finite-difference approximations, to represent linear ageostrophic Kelvin waves and continental shelf waves. This geometry also allows the formulation of basic geophysical fluid dynamical problems involving the interaction of along-channel currents with topography and the extension of that type of problem to cases with mean across-channel bottom slope representative of the topographic constraint of the continental margin. In fact, the periodic channel provides a basic geometry for process studies in idealized coastal numerical models (e.g., Haidvogel and Brink 1986).

The eight intermediate models that we evaluate for the periodic channel are a subset of the twelve included in Part II. Those considered here include the balance equations (BE), the balance equations based on momentum equations (BEM), the potential vorticity conserving linear balance equations (LQBE), the related hybrid balance equations (HBE) and near balance equations (NBE), a geostrophic vorticity (GV) approximation, the geostrophic momentum (GM) approximation, and the quasi-geostrophic momentum and full continuity equations (IM). The models LQBE, BEM, HBE and NBE were formulated and presented in Part I. The selection of the particular intermediate models included here is based on the outcome of the comparisons in Parts I and II and on considerations concerning wall boundary condition application. The models that consistently performed the best in the numerical solutions in Part II were BE and BEM. One of the better models in addition to BE and BEM was LQBE. These models are naturally considered here. On the other hand, NBE and HBE are included because their formulation involves momentum equations and it was felt that consideration of methods for the application of wall boundary conditions for HBE and NBE might help clarify that issue for all of the balance-equation–type models. The GM model is included because it is one of the more well known and frequently applied intermediate models (e.g., Hoskins 1982). Finally, GV and IM are added because the formulations of these models for numerical solution in physical coordinates are perhaps the simplest of all of the intermediate models. In addition, the governing equations for GM, GV, and IM take the form of a generalized QG model and reduce clearly to the QG equation in the appropriate limit.

The outline of this paper is as follows. In section 2, we recall the shallow-water equations (SWE). In section 3 we review QG and the intermediate models and discuss the application of wall boundary conditions. In section 4, the ability of the models to represent ageostrophic Kelvin and topographic waves is tested with numerical solutions. In section 5, initial-value problems involving the interaction of uniform flow in a channel with isolated topographic bumps, both with and without mean across-channel bottom slopes, are utilized for the comparison of model and SWE solutions. The results are summarized in section 6. The numerical methods are given in appendix A and additional discussion of the BEM model is included in appendix B.

2. Shallow-water equations

We examine rotating fluid flows governed by the shallow-water equations (SWE) on an *f*-plane. Dimensionless variables similar to those in Pedlosky (1987)

are utilized so that in Cartesian coordinates (x, y) the continuity and momentum equations are

$$\epsilon F\eta_t + (hu)_x + (hv)_y = 0, \quad (2.1a)$$

$$\epsilon u_t + \epsilon(uu_x + vu_y) - v = -\eta_x + G^{(u)}, \quad (2.1b)$$

$$\epsilon v_t + \epsilon(uv_x + vv_y) + u = -\eta_y + G^{(v)}, \quad (2.1c)$$

where

$$h = \epsilon F\eta + 1 - h_B, \quad (2.1d)$$

$\epsilon F\eta$ is the elevation of the free surface relative to the undisturbed depth of the fluid $H = 1 - h_B$ where $h_B(x, y)$ is the height of the bottom topography, (u, v) are velocity components in the (x, y) directions, G is a generic representation of horizontal friction terms with a superscript to denote the equation, and t is time. Subscripts (x, y, t) denote partial differentiation. There are two dimensionless parameters, the Rossby number ϵ and F,

$$\epsilon = U/(fL), \quad F = f^2L^2/(g\mathcal{D}), \quad (2.2a,b)$$

where L, $\mathcal{D}$, and U are characteristic values for, respectively, a horizontal scale, the undisturbed fluid depth, and a horizontal fluid velocity, f is the Coriolis parameter, and g is the acceleration of gravity. The parameter F is the square of the ratio of the horizontal length scale L to the Rossby radius of deformation $\delta_R = (g\mathcal{D})^{1/2}/f$. As in Pedlosky (1987), the dimensionless variables (x, y), t, (u, v), h_B, and η have been formed from their dimensional counterparts by using the characteristic scales L, L/U, U, $\mathcal{D}$, and $\epsilon F\mathcal{D}$, respectively.

We will also utilize (2.1a,b,c) in the equivalent forms

$$\epsilon F\eta_t + (\hat{H}u)_x + (\hat{H}v)_y + D = 0, \quad (2.3a)$$

$$\epsilon u_t - (1 + \epsilon\zeta)v = -\mathcal{B}_x + G^{(u)}, \quad (2.3b)$$

$$\epsilon v_t + (1 + \epsilon\zeta)u = -\mathcal{B}_y + G^{(v)}, \quad (2.3c)$$

where

$$\mathcal{B} = \eta + \epsilon K, \quad K = \tfrac{1}{2}(u^2 + v^2), \quad (2.3d,e)$$

$$\hat{H} = \epsilon F\eta - h_B, \quad (2.3f)$$

$$\zeta = v_x - u_y, \quad D = u_x + v_y, \quad (2.3g,h)$$

$\mathcal{B}$ is the Bernoulli function, ζ is the vertical component of relative vorticity, and D is the horizontal divergence.

Equations for ζ and D follow from (2.3b,c):

$$\epsilon(\zeta_t + u\zeta_x + v\zeta_y) + (\epsilon\zeta + 1)D = G^{(\zeta)}, \quad (2.4)$$

$$\epsilon[D_t + uD_x + vD_y + D^2 + 2(v_xu_y - v_yu_x)] - \zeta = -\nabla^2\eta + G^{(D)}, \quad (2.5)$$

where ∇^2 is the horizontal Laplacian operator. The combination of (2.1a) and (2.4) gives

$$Q_t + uQ_x + vQ_y = G^{(Q)}, \quad (2.6)$$

where

$$Q = (1 + \epsilon\zeta)/h, \quad (2.7)$$

is the potential vorticity which, when $G^{(Q)} = 0$, is conserved following fluid particles moving with velocity (u, v). The combination of (2.6) multiplied by hQ and (2.1a) multiplied by Q^2 yields an equation for the potential enstrophy density hQ^2,

$$(hQ^2)_t + (uhQ^2)_x + (vhQ^2)_y = G^{(Q^2)}. \quad (2.8)$$

An additional useful equation

$$Q_{Lt} + (uQ_L)_x + (vQ_L)_y = G^{(Q_L)}, \quad (2.9a)$$

for

$$Q_L = \zeta - \tilde{H}, \quad (2.9b)$$

where

$$\tilde{H} = \hat{H}/\epsilon = F\eta - \epsilon^{-1}h_B, \quad (2.9c)$$

follows from the subtraction of (2.3a) from (2.4).

In the absence of dissipation ($G^{(u,v)} = 0$), the SWE (2.1) also imply the following relation expressing the conservation of energy,

$$\epsilon\left(hK + \frac{1}{2}F\eta^2\right)_t + (uh\mathcal{B})_x + (vh\mathcal{B})_y = 0. \quad (2.10)$$

Initial–boundary-value problems for (2.1) require the specification at $t = 0$ of $u(x, y, 0)$, $v(x, y, 0)$, and $\eta(x, y, 0)$ and the vanishing of the normal component of velocity at rigid boundaries.

We consider motion in a periodic channel of uniform width. The x-axis is aligned in the along-channel direction. The walls of the channel are at $y = 0$, 1, so that the dimensionless width $L^{(y)} = 1$. The flow is periodic in x with period $L^{(x)}$. The boundary conditions are

$$v = 0, \quad \text{at} \quad y = 0, 1, \quad (2.11)$$

and periodicity for all variables in x, e.g.,

$$\eta(x = 0) = \eta(x = L^{(x)}). \quad (2.12)$$

An integral constraint, corresponding to the conservation of mass,

$$\int_0^{L^{(x)}}\int_0^1 \eta_t dxdy = 0, \quad (2.13)$$

follows from the area integral of (2.1a) with boundary conditions (2.11) and (2.12). Likewise, in the frictionless case $G^{(u,v)} = 0$, integration of (2.3b) along the channel walls gives, with (2.11),

$$\int_0^{L^{(x)}} u_t dx = 0, \quad \text{at} \quad y = 0, 1, \quad (2.14)$$

which expresses the conservation of circulation on each boundary.

The horizontal friction terms are biharmonic in the x direction only (Haidvogel and Brink 1986), i.e.,

$$G^{(u)} = -\nu u_{xxxx},\ G^{(v)} = -\nu v_{xxxx}. \quad (2.15a,b)$$

The friction terms are utilized to help provide some weak dissipation of potential enstrophy at high wavenumbers. The viscosity ν is chosen to be small enough that the energetic scales of motion are essentially unaffected.

We choose the parameter $F = 16$ for the numerical solutions presented here so that the dimensionless Rossby radius is less than the channel width, i.e., so $F^{-1/2} = 0.25 < 1$. This, of course, is not typical for barotropic motion over the continental shelf and slope where generally $F^{-1/2} \gg 1$. We are primarily interested in the ultimate application of intermediate models to the continuously stratified case, where the internal Rossby radii of deformation are typically smaller than the shelf-slope width. The choice $F^{-1/2} < 1$ is made here so that the dynamics in the SWE will be closer to that in the stratified case, i.e., so that the effects of vortex stretching due to interface deformations will be an integral part of the flow processes studied.

The numerical finite-difference approximations are discussed in appendix A. Two different numerical models for the shallow-water equations, (SWE) and (SW2), are utilized in the numerical solution intercomparisons to provide a check on the reference solution and to provide a measure of error introduced by variations in finite-difference formulations.

3. Models

We are interested in approximate solutions to the SWE (2.1) in the limiting case of small Rossby number, $\epsilon \ll 1$, with $F = O(1)$. The standard approximation in this case is the quasi-geostrophic (QG) model (Pedlosky 1987) which involves the assumptions that $\epsilon F\eta = O(\epsilon)$ and $h_B = O(\epsilon)$. One objective of intermediate models is to represent small Rossby number flows with $O(1)$ variations in h, i.e., with $\epsilon F\eta = O(1)$ and/or $h_B = O(1)$. Descriptions of the model equations, including the formulations utilized for the application of numerical solution procedures and wall boundary conditions, are given in this section. The numerical finite-difference approximations are discussed in appendix A. All of the intermediate models considered here have continuity equations and corresponding wall boundary conditions such that the mass conservation integral constraint (2.13) is satisfied. The numerical approximations are likewise formulated so that this constraint is preserved in finite-difference form. More detailed descriptions of the intermediate models are given in Part I.

a. Quasi-geostrophic model (QG)

The QG model is derived in Pedlosky (1987) by expanding the variables in an asymptotic expansion in powers of ϵ. The velocity components are geostrophic to leading order,

$$u_G = -\eta_y, \quad v_G = \eta_x, \quad (3.1a,b)$$

and the geostrophic vorticity is

$$\zeta_G = v_{Gx} - u_{Gy} = \nabla^2\eta. \quad (3.2)$$

The flow is governed by the equation

$$Q_{0t} + u_G Q_{0x} + v_G Q_{0y} = G^{(Q_0)}, \quad (3.3a)$$

for quasi-geostrophic potential vorticity,

$$Q_0 = \zeta_G - F\eta + \epsilon^{-1}h_B, \quad (3.3b)$$

which expresses (with $G^{(Q_0)} = 0$) the conservation of Q_0 following fluid particles moving with velocities (u_G, v_G). Written in terms of η, (3.3a) is

$$(\nabla^2\eta - F\eta)_t = -J(\eta, \nabla^2\eta + \epsilon^{-1}h_B) + G^{(Q_0)}, \quad (3.4)$$

where the operator $J(a, b) = a_x b_y - b_x a_y$ is the Jacobian.

Initial-value problems require the specification at $t = 0$ of $\eta(x, y, 0)$. At the wall boundaries, the no normal flow conditions (2.12) imply

$$v_G = 0, \quad \text{at} \quad y = 0, 1. \quad (3.5)$$

In terms of η, (3.5) are

$$\eta = C_1(t), \quad \text{at} \quad y = 0, \quad (3.6a)$$

$$\eta = C_2(t), \quad \text{at} \quad y = 1, \quad (3.6b)$$

where C_1 and C_2 are chosen so that (McWilliams 1977),

$$\int_0^{L^{(x)}} \int_0^1 \eta_t dxdy = 0, \quad (3.7a)$$

and

$$\int_0^{L^{(x)}} dx\eta_{yt} = -\int_0^{L^{(x)}} dx\epsilon^{-1}G^{(u_G)} = 0 \quad \text{at} \quad y = 0. \quad (3.7b)$$

Note that (3.7a,b) and (3.4) imply

$$\int_0^{L^{(x)}} dx\eta_{yt} = 0, \quad \text{at} \quad y = 1, \quad (3.7c)$$

so the integral constraints corresponding to conservation of mass (3.7a) and to the conservation of circulation on each boundary (3.7b,c), similar to (2.13) and (2.14) for the SWE, are maintained.

b. Intermediate model (IM)

The full continuity equation (2.1a) is utilized along with the approximate momentum equations,

$$\epsilon u_{Gt} - \epsilon\zeta_G v_G - v = -\mathcal{B}_{Gx} + G^{(u_G)}, \quad (3.8a)$$

$$\epsilon v_{Gt} + \epsilon\zeta_G u_G + u = -\mathcal{B}_{Gy} + G^{(v_G)}, \quad (3.8b)$$

where

$$\mathcal{B}_G = \eta + \epsilon K_G, \quad K_G = \tfrac{1}{2}(u_G^2 + v_G^2). \quad (3.8c,d)$$

A single governing equation for η is obtained by substituting the expressions for u and v from (3.8a,b) in the continuity equation (2.1a):

$$(h\eta_{xt})_x + (h\eta_{yt})_y - F\eta_t = -\epsilon^{-1}J(h, \mathcal{B}_G) - J(\eta, h\zeta_G) + G^{(\eta)}. \quad (3.9)$$

Initial-value problems require the specification of $\eta(x, y, 0)$. The no normal flow boundary conditions (2.11) are applied to (3.9) by setting $v = 0$ in (3.8a) to obtain an equation involving η alone. These conditions are straightforward to implement in finite-difference form in the governing equation for η (3.9) since it is derived from the continuity equation (2.1a) (see appendix A). The x-integral of (3.8a) along the channel walls where $v = 0$ gives

$$\int_0^{L^{(x)}} u_{Gt}dx + \int_0^{L^{(x)}} v_G u_{Gy}dx = 0, \quad \text{at} \quad y = 0, 1, \quad (3.10)$$

so that there is no analogue in IM to the conservation of boundary circulation as in (2.14) for the SWE.

c. Geostrophic vorticity (GV)

In GV, the continuity equation (2.1a) is utilized along with the approximate momentum equations,

$$\epsilon u_{Gt} - (\epsilon\zeta_G + 1)v = -\mathcal{B}_{Gx} + G^{(u_G)}, \quad (3.11a)$$

$$\epsilon v_{Gt} + (\epsilon\zeta_G + 1)u = -\mathcal{B}_{Gy} + G^{(v_G)}. \quad (3.11b)$$

The vorticity equation that follows from (3.11a,b) combines with (2.1a) to give

$$Q_{Gt} + uQ_{Gx} + vQ_{Gy} = G^{(Q_G)}, \quad (3.12a)$$

which implies the conservation of geostrophic potential vorticity

$$Q_G = (1 + \epsilon\zeta_G)/h, \quad (3.12b)$$

following fluid particles moving with velocities (u, v) (3.11). The combination of (3.12) and (2.1a) yields an equation for the conservation (with $G^{(Q_G)} = 0$) of geostrophic potential enstrophy density hQ_G^2. In general, potential enstrophy conservation follows in the absence of dissipation for all intermediate models that retain (2.1a) and that have an analogue of potential vorticity conservation on fluid particles such as (3.12).

One equation for η is obtained by substituting u and v from (3.11) in (2.1a),

$$(h_G\eta_{xt})_x + (h_G\eta_{yt})_y - F\eta_t = -\epsilon^{-1}J(h_G, \mathcal{B}_G) + G^{(\eta)}, \quad (3.13a)$$

where

$$h_G = h/(1 + \epsilon\zeta_G). \quad (3.13b)$$

Initial-value problems require $\eta(x, y, 0)$. The wall boundary conditions (2.11) are applied to (3.13) by setting $v = 0$ in (3.11a) from which we also obtain

$$\int_0^{L^{(x)}} u_{Gt}dx = 0, \quad \text{at } 0, 1. \quad (3.14)$$

Thus, the circulation along the boundaries of the geostrophic velocity is conserved in analogy to (2.14) for the SWE and similar to (3.7c) for QG and consistent with an area integral of the GV vorticity equation.

d. Geostrophic momentum (GM)

In GM (Hoskins 1975), advection of momentum, represented by the geostrophic values u_G and v_G, by the full u and v velocities is retained so that (2.1b,c) are approximated by

$$\epsilon(u_{Gt} + uu_{Gx} + vu_{Gy}) - v = -\eta_x + G^{(u_G)}, \quad (3.15a)$$

$$\epsilon(v_{Gt} + uv_{Gx} + vv_{Gy}) + u = -\eta_y + G^{(v_G)}. \quad (3.15b)$$

Separate expressions for u and v may be obtained by algebraic manipulation of (3.15):

$$u = (1 + \epsilon\zeta_{GM})^{-1}[-\mathcal{B}_{Gy} - \epsilon v_{Gt} + \epsilon^2(u_{Gy}v_{Gt} - v_{Gy}u_{Gt}) + G^{(v_G)}], \quad (3.16a)$$

$$v = (1 + \epsilon\zeta_{GM})^{-1}[\mathcal{B}_{Gx} + \epsilon u_{Gt} + \epsilon^2(v_{Gx}u_{Gt} - u_{Gx}v_{Gt}) - G^{(u_G)}], \quad (3.16b)$$

where

$$\zeta_{GM} = \zeta_G + \epsilon J(u_G, v_G). \quad (3.17)$$

An equation for ζ_{GM} follows directly from (3.16) by forming D from u and v:

$$\epsilon(\zeta_{GMt} + u\zeta_{GMx} + v\zeta_{GMy}) + (\epsilon\zeta_{GM} + 1)D = G^{(\zeta_{GM})}. \quad (3.18)$$

The combination of (3.18) and (2.1a) gives

$$Q_{GMt} + uQ_{GMx} + vQ_{GMy} = G^{(Q_{GM})}, \quad (3.19a)$$

which expresses, when $G^{(Q_{GM})} = 0$, the conservation of geostrophic momentum potential vorticity

$$Q_{GM} = (1 + \epsilon\zeta_{GM})/h, \quad (3.19b)$$

following fluid particles moving with velocities (u, v) (3.16).

A single equation for η is obtained by substituting (3.16a,b) in (2.1a):

$$(h_{GM}\eta_{xt})_x + (h_{GM}\eta_{yt})_y - F\eta_t + \epsilon J(\eta_x, h_{GM}\eta_{yt}) - \epsilon J(\eta_y, h_{GM}\eta_{xt}) = -\epsilon^{-1}J(h_{GM}, \mathcal{B}_G) + G^{(\eta)}, \quad (3.20a)$$

where

$$h_{GM} = h/(1 + \epsilon\zeta_{GM}). \quad (3.20b)$$

Initial-value problems require $\eta(x, y, 0)$. The wall boundary conditions (2.11) are applied to (3.20) by setting $v = 0$ in (3.16b). From the latter equations we also obtain

$$\int_0^{L^{(x)}} u_{Gt}dx + \epsilon \int_0^{L^{(x)}} (v_{Gx}u_{Gt} - u_{Gx}v_{Gt})dx = 0,$$

$$\text{at} \quad y = 0, 1, \quad (3.21)$$

which is consistent with the area integral of the GM vorticity equation (3.18), but which is not directly analogous to the conservation of boundary circulation (2.14) for the SWE.

Finally, we note that with no dissipation the GM model, (3.15a,b) and (2.1a), possesses the energy conservation equation

$$\epsilon\left(hK_G + \frac{1}{2}F\eta^2\right)_t + (uh\mathcal{B}_G)_x + (vh\mathcal{B}_G)_y = 0. \quad (3.22)$$

e. Linear balance equations (potential vorticity conserving) (LQBE)

The LQBE model was formulated in Part I. It is close to the linear balance equation LBE model (Gent and McWilliams 1983a), but in addition it possesses an analogue of potential vorticity conservation on fluid particles. In Part II, LQBE was found in general to give substantially more accurate solutions than LBE.

The continuity equation (2.3a) is approximated by

$$\epsilon F\eta_t + [(u_G + \epsilon\chi_x)\hat{H}]_x + [(v_G + \epsilon\chi_y)\hat{H}]_y + \epsilon\nabla^2\chi = 0, \quad (3.23)$$

where

$$D = u_x + v_y = \epsilon\nabla^2\chi. \quad (3.24)$$

As discussed in Part I, it may be assumed that LQBE is derived from the following approximate momentum equations,

$$\epsilon u_{Gt} - \epsilon\zeta_G(v_G + \epsilon\chi_y) - v = -\mathcal{B}_{Gx} + G^{(u_G)}, \quad (3.25a)$$

$$\epsilon v_{Gt} + \epsilon\zeta_G(u_G + \epsilon\chi_x) + u = -\mathcal{B}_{Gy} + G^{(v_G)}, \quad (3.25b)$$

which imply the vorticity equation

$$\zeta_{Gt} + (u_G + \epsilon\chi_x)\zeta_{Gx} + (v_G + \epsilon\chi_y)\zeta_{Gy} + (1 + \epsilon\zeta_G)\nabla^2\chi = G^{(\zeta_G)}. \quad (3.26)$$

Thus, LQBE is governed by (3.23) and (3.26). These combine to give

$$Q_{Gt} + (u_G + \epsilon\chi_x)Q_{Gx} + (v_G + \epsilon\chi_y)Q_{Gy} = G^{(Q_G)}, \quad (3.27)$$

so that, when $G^{(Q_G)} = 0$, Q_G (3.12b) is conserved on particles moving with velocities $(u_G + \epsilon\chi_x, v_G + \epsilon\chi_y)$. LQBE is formulated for numerical solution by eliminating $\nabla^2\chi$ from (3.23) and (3.26) to give

$$(\nabla^2\eta - F\eta)_t = -J(\eta, \zeta_G - \tilde{H}) - \epsilon[\chi_x(\zeta_G - \tilde{H})]_x - \epsilon[\chi_y(\zeta_G - \tilde{H})]_y + G^{(\eta)}, \quad (3.28)$$

so that (3.28) and (3.26) are the governing equations.

Initial-value problems require $\eta(x, y, 0)$. Boundary conditions at the walls are applied by requiring that both

$$v = 0 \quad \text{and} \quad v_G + \epsilon\chi_y = 0, \quad \text{at} \quad y = 0, 1. \quad (3.29a,b)$$

The specification of (3.29a,b) in the momentum equation (3.25a) and in the continuity equation (3.23) gives the appropriate boundary conditions for (3.26) and (3.28). Note that the boundary conditions (3.29a,b) are consistent with the conservation of mass in (3.23) and imply the satisfaction of the integral constraint (2.13). In addition, the application of (3.29a,b) in x-integrals of (3.25a) along the channel walls gives (3.14), which implies the conservation of geostrophic boundary circulation. This is consistent with an area integral of the vorticity equation (3.26) and is analogous to (2.14) for the SWE.

f. Hybrid balance equations (HBE)

We consider the following balance-equation–type models (HBE, BEM, BE, NBE) in an order that makes the discussion of their boundary condition application the easiest. The models HBE, BEM and NBE were formulated in Part I and are close to the balance equations BE (Charney 1955, 1962; Bolin 1955, 1956; Lorenz 1960; Gent and McWilliams 1983a, 1984). In these models, the velocity components are written as the sum of rotational and divergent components

$$u = -\psi_y + \epsilon\chi_x, \quad v = \psi_x + \epsilon\chi_y, \quad (3.30a,b)$$

so that

$$\zeta = v_x - u_y = \nabla^2\psi, \quad (3.31)$$

and D is given by (3.24). The full continuity equation (2.1a) is utilized.

In HBE, approximate momentum balances are obtained by substituting (3.30) in (2.3b,c) and retaining $O(\epsilon)$ terms. Using the notation

$$u_R = -\psi_y, \quad v_R = \psi_x, \quad (3.32a,b)$$

we obtain

$$\epsilon u_{Rt} - \epsilon\zeta v_R - v = -\mathcal{B}_{Rx} + G^{(u_R)}, \quad (3.33a)$$

$$\epsilon v_{Rt} + \epsilon\zeta u_R + u = -\mathcal{B}_{Ry} + G^{(v_R)}, \quad (3.33b)$$

where

$$\mathcal{B}_R = \eta + \epsilon K_R, \quad K_R = \frac{1}{2}(u_R^2 + v_R^2). \quad (3.33c)$$

The divergence equation formed from (3.33) [with (2.15)] reduces exactly to the equation of balance,

$$\zeta = \nabla^2\psi = \nabla^2(\eta + \epsilon K_R) + \epsilon(\zeta u_R)_y - \epsilon(\zeta v_R)_x,$$
$$= \nabla^2\eta - \epsilon 2J(\psi_x, \psi_y), \quad (3.34)$$

as an approximation to (2.5).

Numerical finite-difference solutions of HBE may be obtained by methods similar to those used for BE and BEM (sections 3g,h). Here we utilize an alternative solution procedure which may be formulated by using the momentum equations and substituting u and v from (3.33) in (2.1a), which gives

$$(h\psi_{xt})_x + (h\psi_{yt})_y - F\eta_t = -\epsilon^{-1}J(h, \mathcal{B}_R) - J(\psi, h\zeta_R) + G^{(\psi)}. \quad (3.35)$$

Equations (3.34) and (3.35) form two coupled governing equations for ψ and η. The method employed to solve these equations is discussed in appendix A.

For initial-value problems, $\psi(x, y, 0)$ is specified and $\eta(x, y, 0)$ is found from the solution of (3.34). The wall boundary conditions (2.11),

$$v = \psi_x + \epsilon\chi_y = 0, \quad \text{at} \quad y = 0, 1, \quad (3.36)$$

are applied in (3.35) by setting $v = 0$ in (3.33a), which implies

$$\epsilon u_{Rt} - \epsilon\zeta v_R = -\mathcal{B}_{Rx} + G^{(u_R)}, \quad \text{at} \quad y = 0, 1. \quad (3.37)$$

Again, (3.37) is straightforward to implement in (3.35) since that equation is derived in finite-difference form from the substitution of u and v, as given by (3.33a,b), in the continuity equation (2.1a). Note that boundary condition (3.36), which is important for ageostrophic coastally trapped wave dynamics, is formulated exactly in terms of the approximate momentum equations. On the other hand, the x-integral of (3.33a) gives

$$\int_0^{L^{(x)}} u_{Rt}dx - \int_0^{L^{(x)}} \zeta v_R dx = 0, \quad \text{at} \quad y = 0, 1, \quad (3.38)$$

so that HBE, similar to IM, has no analogue of the conservation of boundary circulation (2.14) in the SWE.

What remains then is the specification of a boundary condition for the balance equation (3.34). In formulating a boundary condition for (3.34) it is useful to see how this must be done in the linear inviscid limit where (3.33) and (2.1a) are approximated by

$$\epsilon u_{Rt} - v = -\eta_x, \quad (3.39a)$$

$$\epsilon v_{Rt} + u = -\eta_y, \quad (3.39b)$$

$$\epsilon F\eta_t + (Hu)_x + (Hv)_y = 0. \quad (3.39c)$$

We know in this case from independent derivation of the linear equations in the f-plane low-frequency limit (e.g., Part I) that

$$u = -\eta_y - \epsilon\eta_{xt}, \quad v = \eta_x - \epsilon\eta_{yt}, \quad (3.40a,b)$$

so that we should find

$$\psi = \eta, \quad \chi = -\eta_t = -\psi_t. \quad (3.41a,b)$$

The vorticity and divergence equations derived from (3.39a,b) are

$$\zeta_t + \nabla^2\chi = 0, \quad \nabla^2\psi = \nabla^2\eta, \quad (3.42a,b)$$

or

$$\nabla^2(\psi_t + \chi) = 0, \quad \nabla^2(\psi - \eta) = 0. \quad (3.42c,d)$$

The momentum equations (3.39a,b), after substitution of (3.30a,b), may be written

$$-\epsilon(\psi_t + \chi)_y = (\psi - \eta)_x, \quad (3.43a)$$

$$\epsilon(\psi_t + \chi)_x = (\psi - \eta)_y. \quad (3.43b)$$

It is clear, since (3.43a,b) are the Cauchy-Riemann conditions for $\epsilon(\psi_t + \chi)$ and $(\psi - \eta)$, that boundary conditions for (3.42c,d) derived from the momentum equations (3.43a,b) alone will not be sufficient to specify unique solutions. For example, if $\epsilon(\psi_t + \chi)$ and $(\psi - \eta)$ satisfy (3.43a,b) and (3.42c,d), then so will

$$\epsilon\chi = -\epsilon\psi_t + a(x, y, t), \quad (3.44a)$$

$$\psi = \eta + b(x, y, t), \quad (3.44b)$$

where a and b are any conjugate harmonic functions such that

$$a_x = b_y, \quad a_y = -b_x, \quad (3.45a,b)$$

$$\nabla^2 a = \nabla^2 b = 0. \quad (3.45c,d)$$

This is the same situation as the non-uniqueness of the solutions for ψ and χ in a bounded region given ζ and D and the no normal flow boundary condition (Gent and McWilliams 1983a). To obtain unique solutions for ψ and χ that agree with (3.41a,b), an additional boundary condition, such as

$$\eta_y = \psi_y, \quad \text{at} \quad y = 0, 1, \quad (3.46)$$

along with the integral condition,

$$\int_0^{L^{(x)}} \int_0^1 (\psi - \eta)dxdy = 0, \quad (3.47)$$

must evidently be specified independently. The conditions (3.46) and (3.47) imply $a = b = 0$ in (3.44) and give (3.41).

For HBE, we choose a condition that reduces to (3.46) in the linear limit and specify the following approximate boundary condition for (3.34) from (3.33b):

$$\eta_y = \psi_y - \epsilon(\zeta u_R + K_{Ry}) \quad \text{on} \quad y = 0, 1, \quad (3.48)$$

along with (3.47).

g. *Balance equations (based on momentum equations) (BEM)*

A model very close to BE was formulated in Part I and may be derived from (2.1a) and the following approximate momentum equations:

$$\epsilon u_{Rt} - (\epsilon\zeta + 1)v = -\mathcal{B}_{Rx} + G^{(u_R)}, \quad (3.49a)$$

$$\epsilon v_{Rt} + (\epsilon\zeta + 1)u = -\mathcal{B}_{Ry} + G^{(v_R)}. \quad (3.49b)$$

These are similar to (3.33) for HBE with the exception that the full u and v are retained here in the rotation terms. The resulting vorticity equation,

$$\zeta_t + u\zeta_x + v\zeta_y + (1 + \epsilon\zeta)\nabla^2\chi = G^{(\zeta)}, \quad (3.50)$$

has the same form as (2.4) for the SWE. The full continuity equation (2.1a) is retained so that (2.1a) and (3.50) combine to give, in the absence of dissipation, conservation of potential vorticity (2.7) following fluid particles moving with velocity (u, v) (3.30) as in (2.6). The divergence or balance equation implied by (3.49a,b) is

$$\zeta = \nabla^2\psi = \nabla^2(\eta + \epsilon K_R) + \epsilon(\zeta u_R)_y - \epsilon(\zeta v_R)_x + \epsilon^2(\zeta\chi_x)_y - \epsilon^2(\zeta\chi_y)_x$$
$$= \nabla^2\eta - \epsilon 2J(\psi_x, \psi_y) - \epsilon^2 J(\zeta, \chi). \quad (3.51)$$

BEM differs from BE solely due to the inclusion of the $\epsilon^2 J(\zeta, \chi)$ term in the divergence equation (3.51) for BEM. The presence of χ in (3.51) adds additional complications to BEM compared to BE and these are discussed further in appendix B.

BEM is solved here by eliminating $\nabla^2\chi$ from (3.50) and (2.3a) to form

$$(\nabla^2\psi - F\eta)_t = -J(\psi, \zeta - \tilde{H}) - \epsilon[\chi_x(\zeta - \tilde{H})]_x - \epsilon[\chi_y(\zeta - \tilde{H})]_y + G^{(\psi)}, \quad (3.52)$$

and by considering (3.50), (3.51) and (3.52) as the governing equations. These are stepped forward in time by using an iterative method as described in appendix A.

For initial-value problems, $\psi(x, y, 0)$ is specified at $t = 0$ (see appendix B). Boundary conditions for (3.50) and (3.52) are obtained from (3.36) and the use of (3.36) in the momentum equation (3.49a) which gives

$$\epsilon u_{Rt} = -\mathcal{B}_{Rx} + G^{(u_R)}, \quad \text{at} \quad y = 0, 1. \quad (3.53)$$

The approximate boundary condition,

$$\eta_y = \psi_y - \epsilon(\zeta u_R + K_{Ry}) - \epsilon^2(\zeta\chi_x), \quad (3.54)$$

for (3.51) is formulated based on the same reasoning as given in connection with (3.48). The x-integral of (3.53) gives

$$\int_0^{L^{(x)}} u_{Rt}\,dx = 0, \quad (3.55)$$

so that the circulation along the boundaries of the rotational component of the velocity is conserved in analogy to (2.14) for the SWE and consistent with an area integral of the vorticity equation (3.50) and boundary condition (3.36).

h. Balance equations (BE)

The balance equations are derived from the SWE by substituting u and v from (3.30) in the vorticity (2.4) and divergence equations (2.5) and retaining $O(1)$ and $O(\epsilon)$ terms. This gives (3.34) and (3.50). The full continuity equation (2.1a) is also utilized and this combines with the vorticity equation (3.50) to give conservation of potential vorticity (2.7) following fluid particles moving with velocity (u, v) (3.20) as in (2.6). We solve BE here by combining (2.3a) and (3.50) to give (3.52) and by considering (3.34), (3.50) and (3.52) to be the governing equations. For initial-value problems, we specify $\psi(x, y, 0)$.

The momentum equations that correspond to the truncation of the vorticity (3.50) and divergence (3.34) equations in BE do not follow directly as approximations to (2.1b,c), but involve implicitly defined force potential correction terms and are referred to as equivalent momentum equations (Gent and McWilliams 1983a). This complicates the application of wall boundary conditions for (3.34), (3.50), and (3.52). In addition to requiring (3.36), we proceed by utilizing, as approximate boundary conditions, (3.53) and (3.48). The errors incurred by use of (3.53) should be of $O(\epsilon^2)$ as indicated, e.g., by the fact that BE and BEM differ only by the additional $O(\epsilon^2)$ terms in (3.51) compared to (3.34). The justification for (3.48) is the same as given in connection with its use in HBE with additional errors of $O(\epsilon^2)$ expected here. The x-integral of (3.53) implies (3.55), consistent with the area integral of (3.50).

i. Near balance equations (NBE)

The NBE model utilizes the continuity equation (2.1a) and approximate momentum equations similar to (3.49a,b) for BEM with the exception that the streamfunction is expanded as

$$\psi = \psi_0 + \epsilon^2\psi_1, \quad (3.56)$$

and we assume

$$\epsilon u_{R0t} - (1 + \epsilon\zeta_{R0})v = -\mathcal{B}_{R0x} + G^{(u_{R0})}, \quad (3.57a)$$

$$\epsilon v_{R0t} + (1 + \epsilon\zeta_{R0})u = -\mathcal{B}_{R0y} + G^{(v_{R0})}, \quad (3.57b)$$

where

$$u_{R0} = -\psi_{0y}, \quad v_{R0} = \psi_{0x}, \quad (3.58a,b)$$

$$\zeta_{R0} = \nabla^2\psi_0, \quad \mathcal{B}_{R0} = \eta + \frac{1}{2}\epsilon(u_{R0}^2 + v_{R0}^2). \quad (3.59a,b)$$

The equation of balance,

$$\nabla^2\psi_0 = \nabla^2\eta - \epsilon 2J(\psi_{0x}, \psi_{0y}), \quad (3.60)$$

which follows from approximating the divergence equation found from (3.57) to $O(\epsilon)$ is also assumed to hold. The vorticity equation implied by (3.57) combines with (2.1a) to give the conservation of NBE potential vorticity $Q_{R0} = (1 + \epsilon\zeta_{R0})/h$ following fluid particles moving with velocities (u, v) (3.57).

Substitution of u and v from (3.57) in (2.1a) gives

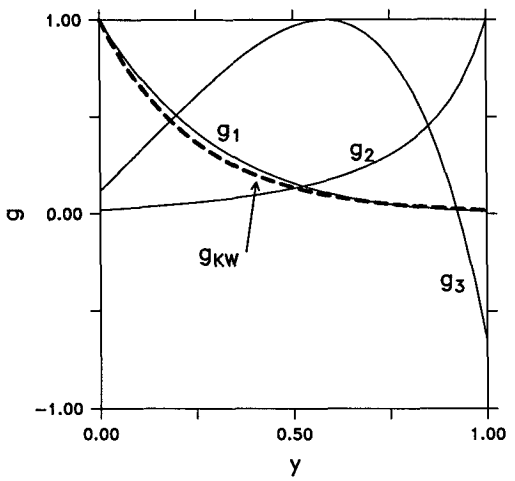

FIG. 1. The y-dependence of the SWE Kelvin wave solution $g_{KW}(y)$ with a flat bottom for $F = 16$ and the first three across-channel modes $g_i(y)$ $i = 1, 2, 3$ with bottom topography (4.15) and $h_W = 0.8$ for $F = 16$ and $k = \pi/4$.

$$(h_{R0}\psi_{0xt})_x + (h_{R0}\psi_{0yt})_y - F\eta_t = -\epsilon^{-1}J(h_{R0}, \mathcal{B}_{R0}) + G^{(\psi_0)}, \quad (3.61a)$$

where

$$h_{R0} = h/(1 + \epsilon\zeta_{R0}). \quad (3.61b)$$

Similar to (3.34) and (3.35) for HBE, (3.60) and (3.61) form two coupled governing equations for η and ψ_0. The method used to obtain numerical solutions is discussed in appendix A.

Initial-value problems require the specification of $\psi_0(x, y, 0)$. Boundary conditions at $y = 0, 1$ for (3.61a) are obtained by setting $v = 0$ in (3.57a). An approximate boundary condition equivalent to (3.48) (with ψ replaced by ψ_0) is utilized for (3.60). The x integral of (3.57a) at $y = 0, 1$ with $v = 0$ implies (3.55) with u_{Rt} replaced by u_{R0t}.

4. Linear ageostrophic waves

The importance of linear ageostrophic coastally trapped wave motion to the behavior of continental shelf flow fields is well known. The capability of intermediate models to represent ageostrophic Kelvin and continental shelf waves was discussed in Part I. It was shown there that in the linear limit the intermediate models discussed in section 3 represent these waves with accuracy consistent with a standard linear low-frequency approximation. In this section, we test that result and verify that our finite-difference formulations of the equations and of the boundary conditions properly admit these waves. Specifically, we present numerical solutions for problems involving the propagation of linear Kelvin waves and the propagation of first mode linear continental shelf waves (with the latter represented by ageostrophic topographic-Rossby waves in a channel). The linear solutions for waves that vary sinusoidally in time and in the along-channel direction are utilized to initialize, for a specified along-channel wavenumber, all of the intermediate models and the SWE. Solution accuracy of the intermediate models is appraised by appropriate comparison with the results for the SWE.

TABLE 1. Rescaled phase velocities $\hat{c}_i = \epsilon c_i = \epsilon\omega_i/k$ for the linear cross-channel wave modes from the solution of (4.11) with constant bottom slope (4.15), $k = \pi/4$ and $F = 16$.

Phase velocity	$h_W = 0.8$	$h_W = 0.3$
$\hat{c}_1$	0.304	0.270
$\hat{c}_2$	−0.143	−0.215
$\hat{c}_3$	−0.062	−0.023
$\hat{c}_4$	−0.032	−0.011

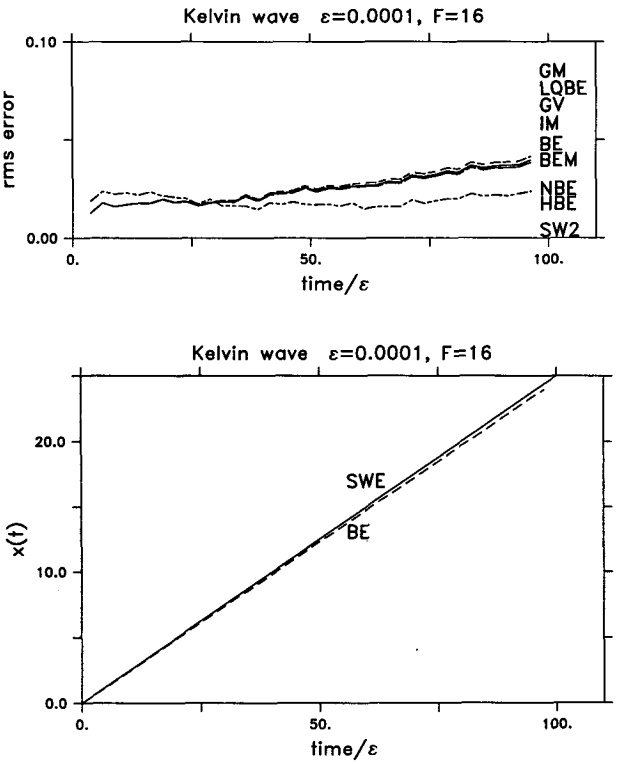

FIG. 2. The rms error (4.18) (top) from the intermediate models and from SW2 compared to SWE for the Kelvin wave problem. The type of line (solid, dashed, etc.) representing the rms error for each model is consistent in Figs. 2, 4, 9, 11, 14, and 16. The correspondence of model and line-type may be seen clearly in Fig. 14. Also (bottom), the (x, t) coordinates of the zero crossing of η (with $\eta_x > 0$) at $y = 0.11$ from SWE (solid line) and from BE (dashed line) for the Kelvin wave problem.

The linear inviscid shallow-water equations for motion over O(1) topographic variations on an f-plane are

$$\epsilon F\eta_t + (Hu)_x + (Hv)_y = 0, \quad (4.1a)$$

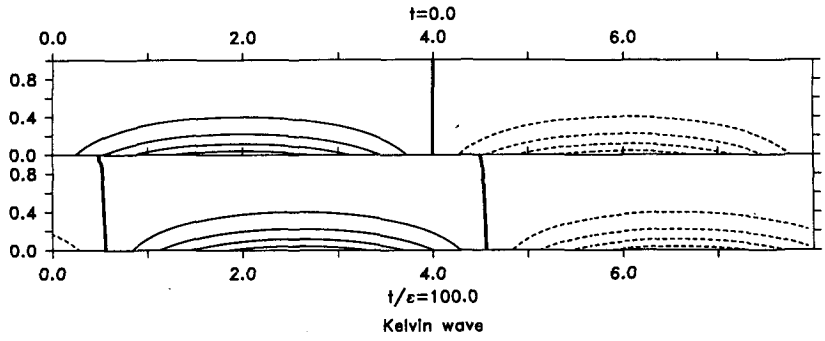

FIG. 3. Contours of the η field for the Kelvin wave problem from BE at $t = 0$ and at $t = t_F = 100\epsilon = 0.01$. The contour interval is 0.2. The zero contour line is heavy. The solid (dashed) contour lines are for positive (negative) values.

$$\epsilon u_t - v = -\eta_x, \tag{4.1b}$$

$$\epsilon v_t + u = -\eta_y. \tag{4.1c}$$

It follows from (4.1b,c) that

$$\mathcal{L}u = -\eta_y - \epsilon\eta_{xt}, \quad \mathcal{L}v = \eta_x - \epsilon\eta_{yt}, \tag{4.2a,b}$$

where

$$\mathcal{L} = 1 + \epsilon^2\partial^2/\partial t^2. \tag{4.2c}$$

Substituting (4.2a,b) in $\mathcal{L}$ (4.1a), we obtain a single equation for η:

$$[(H\eta_x)_x + (H\eta_y)_y - F\mathcal{L}\eta]_t = -\epsilon^{-1}J(\eta, h_B). \tag{4.3}$$

The boundary conditions (2.12) from (4.2b) are

$$\eta_x - \epsilon\eta_{yt} = 0, \quad \text{at} \quad y = 0, 1. \tag{4.4}$$

For all of the intermediate models in section 3, the following single governing equation for η may be found in the linear limit (Part I):

$$[(H\eta_x)_x + (H\eta_y)_y - F\eta]_t = -\epsilon^{-1}J(\eta, h_B). \tag{4.5}$$

In addition, the velocity components are given by (3.40a,b), i.e., by (4.2a,b) with $\mathcal{L}$ replaced by 1, so that the wall boundary condition is also (4.4).

First, we consider Kelvin waves over a flat bottom ($h_B \equiv 0$) with solutions of the form

$$\eta = C\exp(-i\omega t + ikx - ry), \tag{4.6}$$

so that there is exponential decay into the channel from $y = 0$ and propagation toward positive x. For the SWE (4.3), we obtain

$$r = r_S = F^{1/2}, \quad \epsilon\omega = \epsilon\omega_S = k/r_S, \tag{4.7a,b}$$

whereas for the intermediate models,

$$r = r_I = (k^2 + F)^{1/2}, \quad \epsilon\omega = \epsilon\omega_I = k/r_I. \tag{4.8a,b}$$

The velocity components,

$$u = -\eta_y = r\eta, \quad v = 0. \tag{4.9a,b}$$

Note that the intermediate models distort the SWE dispersion relation (4.7b) by the difference between r_I and r_S and require $k^2 \ll F$ for accurate Kelvin wave approximation.

For the topographic waves, we assume $h_B = h_B(y)$ and let

$$\eta = g(y)\exp(-i\omega t + ikx). \tag{4.10}$$

For simplicity in obtaining the cross-channel modes g, we assume the low-frequency limit $(\epsilon\omega^2) \ll 1$ in (4.3) and find the solutions to (4.5). In that case,

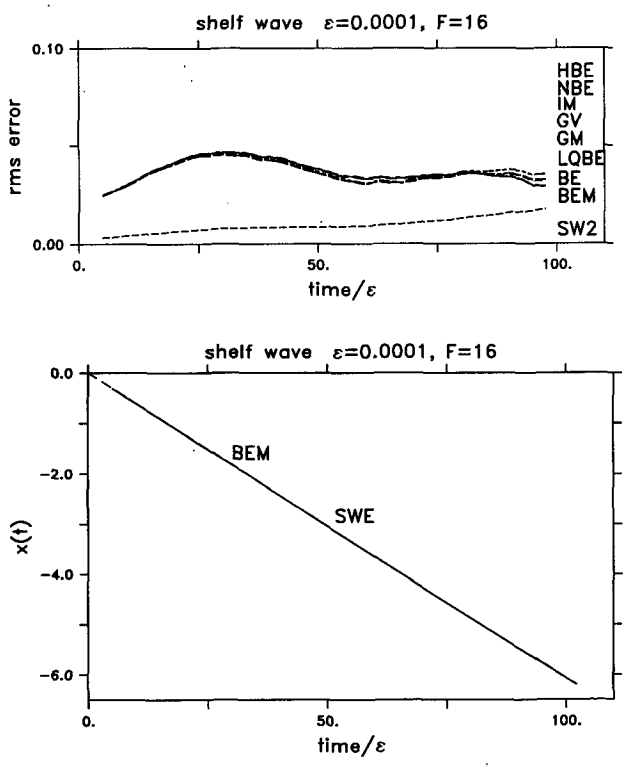

FIG. 4. The rms error (4.18) (top) from the intermediate models and from SW2 compared to SWE for the topographic wave problem. Also (bottom), the (x, t) coordinates of the zero crossing of η (with $\eta_x < 0$) at $y = 0.48$ from SWE (solid line) and from BEM (dashed line) for the topographic wave problem.

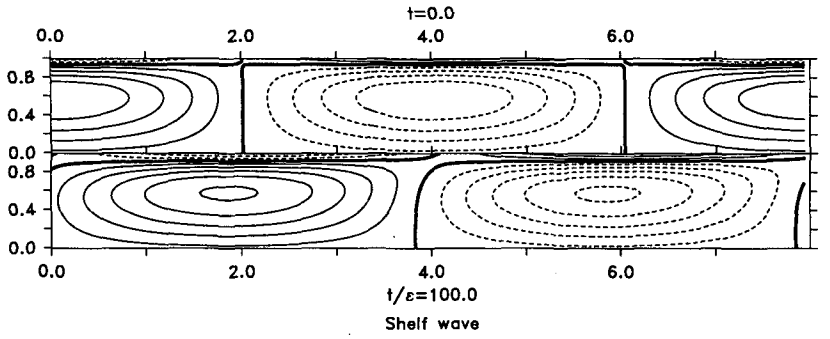

FIG. 5. Contours of the η field for the topographic wave problem from BEM at $t = 0$ and at $t = t_F = 100\epsilon = 0.01$. The contour interval is 0.2. The zero contour line is heavy. The solid (dashed) contour lines are for positive (negative) values.

$$g_{yy} + sg_y + (-k^2 + sb^{-1} - FH^{-1})g = 0, \quad (4.11)$$

where

$$s = H_y/H, \quad b = \epsilon\omega/k. \quad (4.12a,b)$$

The boundary conditions for (4.11) from (4.4) are

$$g + bg_y = 0, \quad \text{at} \quad y = 0, 1. \quad (4.13)$$

The velocity components are given by

$$(u, v) = [(-g_y - \epsilon\omega kg), i(kg + \epsilon\omega g_y)] \times \exp(-i\omega t + ikx). \quad (4.14a,b)$$

For these calculations we specify $F = 16$, $k = \pi/4$, $L^{(y)} = 1$, $L^{(x)} = 8$ with grid spacing $\Delta y = 1/32$ and $\Delta x = 2\Delta y$, so that the total number of interior grid points is equal to 32×128. The viscosity $\nu = 5 \times 10^{-9}$. We present one set of results for a Kelvin wave and one set for what is essentially the first mode topographic wave. For the topographic waves we utilize a constant bottom slope,

$$h_B = 2h_W(y - 0.5), \quad (4.15)$$

where $h_W = 0.8$ and $dh_B/dy = 1.6$.

The Rossby number ϵ is chosen to be small but finite ($\epsilon = 10^{-4}$), so that the motion will be nearly linear but will be governed by the full nonlinear equations. For the Kelvin waves, we initialize BE, BEM, NBE, and HBE by assuming the linear solution for η, (4.6) and (4.7), is equal to an initial streamfunction $\Psi_I(x, y)$. The initial value $\eta(x, y, 0)$ is then obtained from the solution of the various balance equations. Since $\epsilon = 10^{-4}$ is small, $\Psi_I(x, y)$ and $\eta(x, y, 0)$ are nearly equal. The models LQBE, GV, GM and IM are initialized with $\eta(x, y, 0)$ from BE. The SWE and SW2 are initialized with $\eta(x, y, 0)$ from BE and with velocity components calculated from (3.30a,b) where $\psi(x, y, 0) = \Psi_I(x, y)$ and $\chi(x, y, 0)$ is found from the BE solution. For the topographic waves, the initial values are found in the same way starting with the assumption that the linear solution for η, with $g(y)$ obtained from (4.11), is equal to $\Psi_I(x, y)$.

In Fig. 1 we show the y-dependence of the initial SWE Kelvin wave solution $g_{KW} = \exp(-F^{1/2}y)$. The rescaled propagation velocity $\hat{c}_{KW} = \epsilon c_{KW} = \epsilon\omega/k = F^{-1/2} = 0.25$. For the topographic waves, we find $g_i(y)$ and $\hat{c}_i = \epsilon c_i = \epsilon\omega_i/k$ from the numerical solution of (4.11) with boundary condition (4.13), where the subscript $i = 1, 2, \cdots$ denotes mode number and the modes are ordered so that the absolute values of rescaled wave speeds $\hat{c}_i$ decrease as i increases. In Fig. 1, we also plot $g_i(y)$ for the first three modes with $k = \pi/4$, $F = 16$ and h_B given by (4.15) with $h_W = 0.8$. The modes are normalized so that the maximum absolute value of $g_i(y)$ is equal to one. The corresponding values of $\hat{c}_i$ for the first four modes are given in Table 1. Also

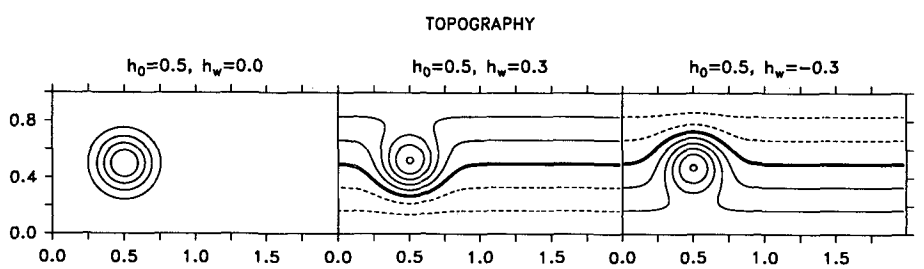

FIG. 6. Contours of the channel bottom topography used in cases 1–4 (Table 2) where $L^{(x)} = 2$, $h_0 = 0.5$ and $h_W = 0.0$, +0.3, and −0.3. The contour interval is 0.1. The zero contour line is heavy. The solid (dashed) contour lines are for positive (negative) values.

TABLE 2. Parameter values for the initial-value problems involving flow over topography. In all cases, $F = 16$ and $\nu = 5 \times 10^{-9}$.

Case	ϵ	h_0	h_W
1	0.001	0.5	0
2	0.005	0.5	0
3	0.005	0.5	0.3
4	0.005	0.5	−0.3

listed in Table 1 are the values of $\hat{c}_i$ for the first four modes with $h_W = 0.3$, which corresponds to a geometry utilized in some of the calculations in section 5.

From Fig. 1 and Table 1, we see that the first two modes g_1 and g_2 correspond to topographically modified Kelvin waves with one mode decaying into the interior from each wall and with propagation for each mode in the appropriate direction. The third mode, which has the characteristic structure in $g_3(y)$ of a first-mode topographic wave is used to initialize the topographic wave calculations. An examination of the y-dependence of η and of v, i.e., of g_3 and $(g_3 + \hat{c}_3 g_{3y})$ from (4.14b), shows substantial differences indicating that the $\hat{c}_3 g_{3y}$ term in v is not small relative to g_3 and thus that the waves are ageostrophic. For comparison, the QG solutions for topographic wave modes in a channel with constant bottom slope, obtained from (4.10)–(4.14) in the limit $s \ll 1$, $b \ll 1$, $sb^{-1} = O(1)$, are

$$g_{n\mathrm{QG}}(y) = C_n \sin(n\pi y) \quad n = 1,2, \cdots, \tag{4.16}$$

with

$$\hat{c}_{n\mathrm{QG}} = \epsilon\omega_n/k = \frac{-kh_{By}}{[k^2 + (n\pi)^2 + F]}. \tag{4.17}$$

For $k = \pi/4$, $F = 16$, $h_{By} = 1.6$, $n = 1$, (4.17) gives $\hat{c}_{1\mathrm{QG}} = -0.047$ which differs considerably from $\hat{c}_3 = -0.062$ in Table 1. Likewise the normalized structure, $g_{1\mathrm{QG}} = \sin(\pi y)$, differs from g_3 in Fig. 1.

To evaluate the accuracy of the model solutions we use a measure of error based on the difference in the free surface elevation η of the model and of SWE. Integration over the model domain and normalization by the root mean square of η in SWE, gives the fractional measure,

$$\text{rms error} = \left\{ \frac{\Sigma\,[\eta(\mathrm{SWE}) - \eta]^2}{\Sigma\,[\eta(\mathrm{SWE}) - \langle\eta(\mathrm{SWE})\rangle]^2} \right\}^{1/2}, \tag{4.18}$$

where the summation is over all grid points in the domain and the angle brackets indicate a spatial mean value. We use this measure of error in Part II as well as in all of the numerical experiments here. One difficulty in comparing the values of other variables, such as vorticity or potential vorticity, to assess accuracy is that these quantities have different definitions in the different models. The free surface elevation η, however, is a variable common to all models and is related through its derivatives to the important geostrophic velocities. We have found by qualitative comparison of other fields, (e.g., see section 5, Fig. 12), that (4.18) appears to give a consistent measure of solution accuracy.

We calculate the wave propagation from $t = 0$ to $t_F = 100\epsilon$ so that the dimensionless time interval t_F corresponds to about 16 inertial periods (in dimensionless time t, the inertial period $T_I = 2\pi\epsilon$). For the Kelvin wave this gives a propagation distance of $L_P = c_{\mathrm{KW}} t_F = 25$. For the slower topographic wave $L_P = c_3 t_F = -6.2$. For the model comparisons in the topographic wave case, the solutions from SWE and SW2 are averaged over an inertial period. This is the procedure used in section 5 and in Part II. For the Kelvin wave comparisons, the unaveraged SWE and SW2 solutions are utilized because the relatively large propagation velocities of the Kelvin waves lead to significant structure changes when averaging is employed.

In the Kelvin wave case, the solutions from SWE, SW2, and all of the intermediate models show essentially nondispersive propagation of the initial wave form in the correct manner. This is illustrated in Fig. 2 where we plot the (x, t) coordinates of the η zero-crossing in x (with $\eta_x > 0$) at $y = 0.11$ from SWE and BE. These form straight lines corresponding to $\epsilon dx/dt = 0.25$ for SWE, in excellent agreement with the theoretical value from (4.7b) $\hat{c}_{\mathrm{KW}} = r_S^{-1} = F^{-1/2} = 0.25$, and to $\epsilon dx/dt = 0.2455$ from BE, which is close to $\hat{c}_I = r_I^{-1} = (k^2 + F)^{-1/2} = 0.2453$ from (4.8b). Time series of the rms error (4.18) are also given in Fig. 2. These rms error time series have been smoothed by using a running average over three sampling time intervals Δt_S, where $\Delta t_S = 2.5\epsilon^{-1}$, to suppress the effects of the small amount of high-frequency variability present in the unaveraged SWE and SW2 solutions. Since $\hat{c}_{\mathrm{KW}}$ differs from $\hat{c}_I$, in calculating (4.18) we adjust the

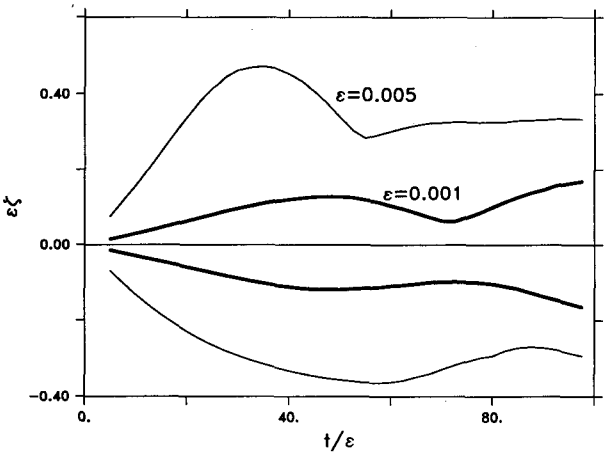

FIG. 7. The maximum and minimum values of $\epsilon_L = \epsilon\zeta$ as a function of time from SWE for case 1 (heavy lines) and for case 2 (light lines).

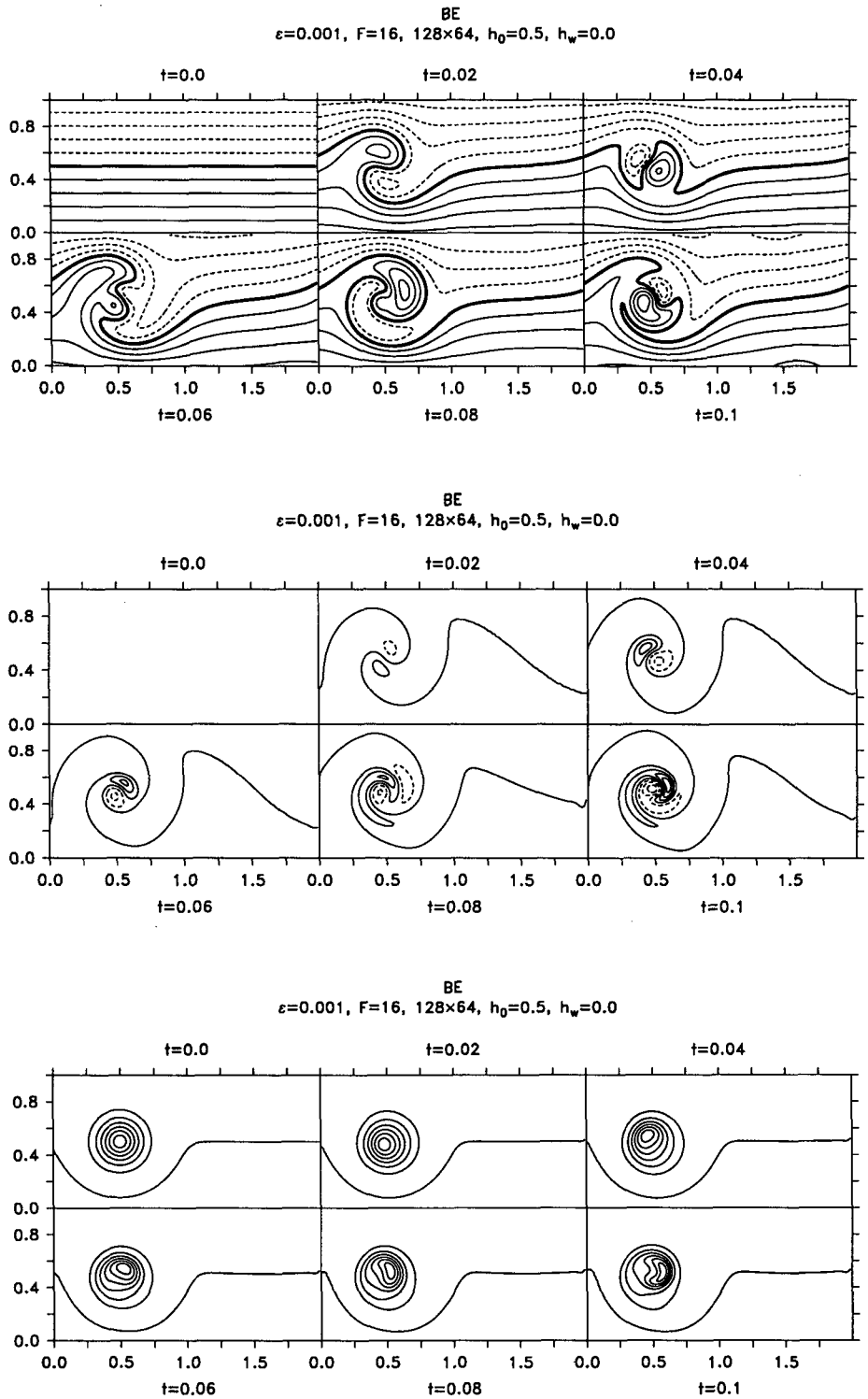

FIG. 8. Contour plots of the η (top), $\epsilon\zeta$ (middle), and Q (bottom) fields at time intervals of 0.02 from BE for case 1. Contour intervals are 0.1 for η, 0.05 for $\epsilon\zeta$, and 0.15 for Q. Solid (dashed) contour lines denote values ≥ 0 (<0). For η, the zero contour line is heavy. For Q, the open contour line is $Q = 1$.

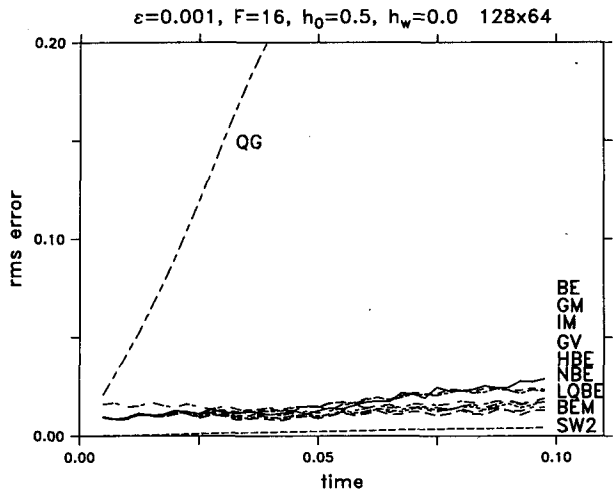

FIG. 9. The rms error (4.18) from the intermediate models, QG, and SW2 compared to SWE for case 1. The type of line representing each model is consistent in Figs. 2, 4, 9, 11, 14, and 16. The correspondence of model and line-type may be seen clearly in Fig. 14.

times so that we compare the SWE and SW2 solutions at $t' = (r_S/r_I)t$ with the intermediate model solutions at t. Contours of the η field at $t = 0$ and at $t = t_F$ from BE are plotted in Fig. 3 and show only small changes in the η wave structure over the time interval of the calculations consistent with linear wave propagation. The time dependence of the errors in Fig. 2 indicates that the models IM, GV, GM, LQBE, BE, and BEM give solutions that behave similarly, as do HBE and NBE, with slight differences between these two groups. The errors of all the models compared to SWE, however, are small. The results show that the intermediate models represent linear ageostrophic Kelvin wave dynamics and that our formulation and implementation in finite-difference form of the wall boundary conditions properly admit linear Kelvin waves. The accuracy of the representation of nonlinear Kelvin waves by the different intermediate models is likewise of interest. The consideration of that question, however, would require substantial additional work to carefully determine the correct reference SWE solutions and is not attempted here.

The errors for the topographic wave experiment are shown in Fig. 4 and contours of the η field at $t = 0$ and at $t = t_F$ from BEM are shown in Fig. 5. We note that the maximum value of the vorticity $|\epsilon\zeta|$ in the initial shelf wave solution with $\epsilon = 10^{-4}$ is 0.05. The numerical solutions from SWE and SW2 and from all of the intermediate models show essentially nondispersive propagation in agreement with the linear wave analytical solutions. This is illustrated in Fig. 4 where the (x, t) coordinates of the η zero-crossing in x (with $\eta_x < 0$) at $y = 0.48$ from SWE and BEM are plotted. These form straight lines corresponding to $\epsilon dx/dt = -0.62$, in agreement with $\hat{c}_3$ (Table 1). The agreement with linear wave theory is also reflected by the generally small, nonincreasing errors in Fig. 4 and by the relatively small changes in the η field of BEM from $t = 0$ to $t = t_F$ in Fig. 5. We conclude, consequently, that the intermediate models properly represent ageostrophic, linear topographic wave dynamics.

5. Flow over topography

In this section we present the results of numerical finite-difference calculations for initial-value problems involving the adjustment of an initially uniform, geostrophically balanced, along-channel flow,

$$u(x, y, t = 0) = 1, \tag{5.1}$$

to a symmetric Gaussian-shaped bottom topographic feature centered between the channel walls. This type of initial-value flow problem might be realized, e.g., in a laboratory experiment involving fluid motion in a rotating annulus that contains bottom topographic variations. Starting with the fluid in equilibrium solid-body rotation with the annulus, a flow adjustment similar to that described by the numerical experiments would take place following a small, step-function change in rotation rate of the annular container. The bottom bump is characterized by a maximum height h_0 at its center and by a width scale L_B and takes the form

$$h_B = h_0 \exp\{-[(x - x_0)^2 + (y - y_0)^2]/L_B^2\}, \tag{5.2}$$

where $x_0 = 0.5$, $y_0 = 0.5$, and $L_B = 0.2$. The length of the channel is $L^{(x)} = 2$. We look at cases where the bottom bump is present in a channel with an otherwise flat bottom and at cases where, in addition, there is a linear across-channel bottom slope given by (4.15) with $h_W = \pm 0.3$. Contour plots of the bottom topography for these three geometries are shown in Fig. 6. The grid size is $\Delta x = \Delta y = 1/64$ so that the total number of grid points is 64×128.

We present the results from four cases. In all of these, the bottom bump height is $h_0 = 0.5$, $F = 16$, and $\nu = 5 \times 10^{-9}$. The four cases include a low Rossby number flow $\epsilon = 0.001$ with a flat bottom $h_W = 0$ and a set of three moderate Rossby number flows at $\epsilon = 0.005$ with $h_W = 0$, $h_W = +0.3$ and $h_W = -0.3$. These are summarized in Table 2.

We initialize the models as follows. From (5.1) and the assumption of geostrophic balance,

$$\eta(x, y, t = 0) = -y + 0.5. \tag{5.3}$$

For BE, BEM, HBE and NBE, with (5.3) the various balance equations imply,

$$\psi(x, y, t = 0) = \eta(x, y, t = 0). \tag{5.4}$$

For SWE and SW2, the initial value of η is given by (5.3) while the initial values of u and v are found from (3.30), with ψ given by (5.4) and $\chi(x, y, t = 0)$ obtained from the solution to BE. We calculate the solutions from $t = 0$ to a final dimensionless time that

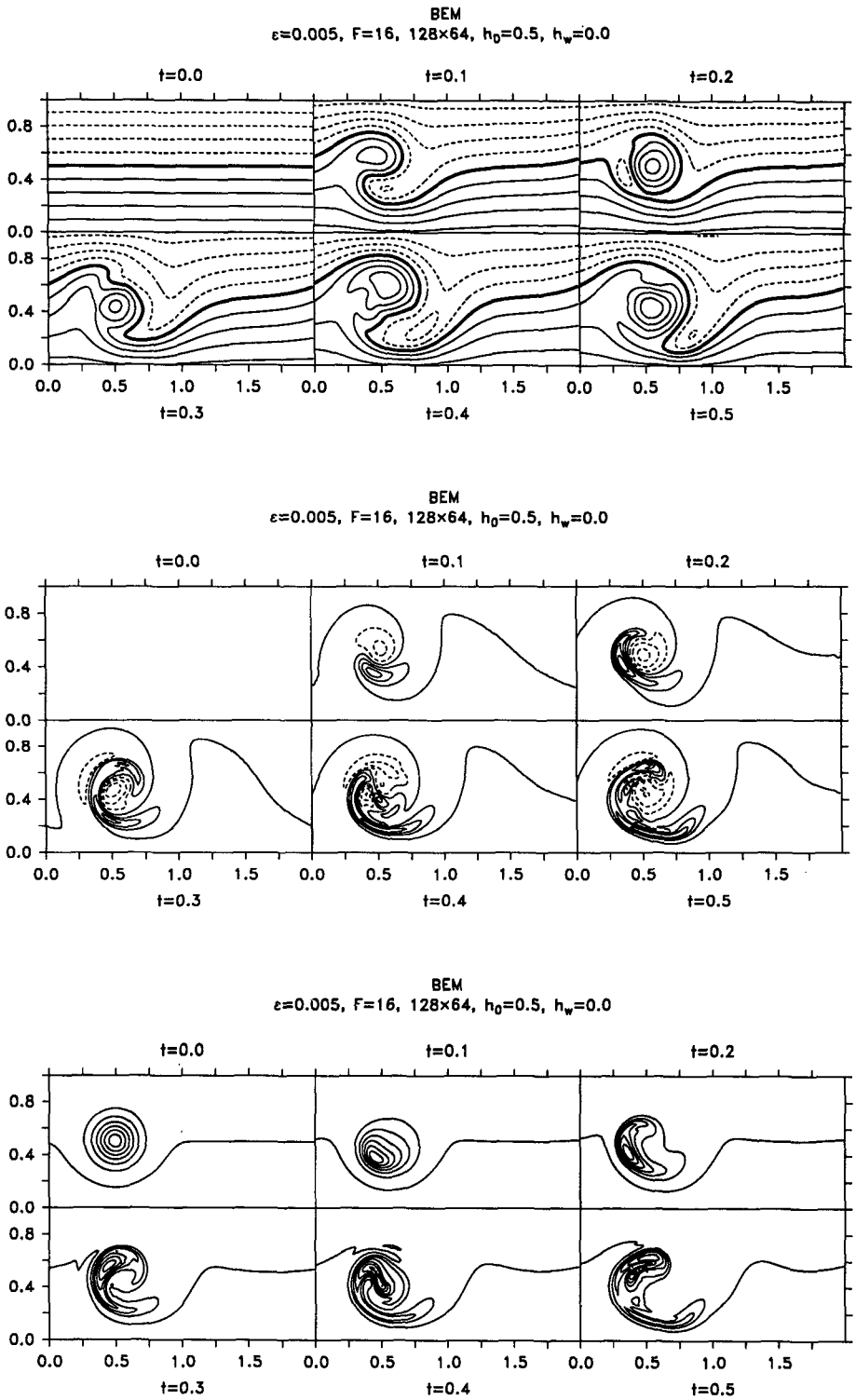

FIG. 10. Contour plots of the η (top), $\epsilon\zeta$ (middle), and Q (bottom) fields at time intervals of 0.1 from BEM for case 2. Contour intervals are 0.1 for η, 0.1 for $\epsilon\zeta$, and 0.15 for Q. Contour lines as in Fig. 8.

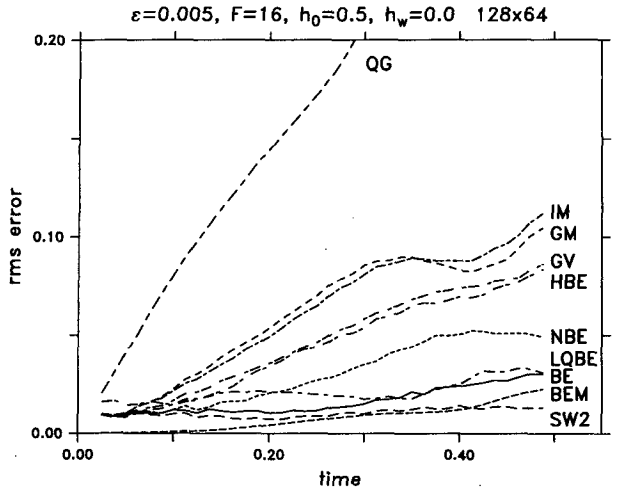

FIG. 11. The rms error (4.18) from the intermediate models, QG, and SW2 compared to SWE for case 2.

corresponds to approximately 16 inertial periods. For comparison with the intermediate models, the solutions from SWE and SW2 are averaged over an inertial period.

For each of the four cases in Table 2, we show the time development of η, ζ and Q with contour plots of these fields at uniform time intervals. In these plots we show the results from BE for case 1, BEM for cases 2 and 3, and SWE for case 4. There are almost no visual differences between the BE and BEM produced η, ζ and Q fields and those from SWE. The BE and BEM results are used to show the intermediate model solutions. We also plot the time variation of the error measure (4.18) for each model compared to SWE. The difference between SWE and SW2 from (4.18) gives an indication of errors due to different numerical finite-difference formulations at this grid resolution. For cases 1 and 2, we also plot in Fig. 7 the maximum and minimum values of $\epsilon_L = \epsilon\zeta$ as a function of time from

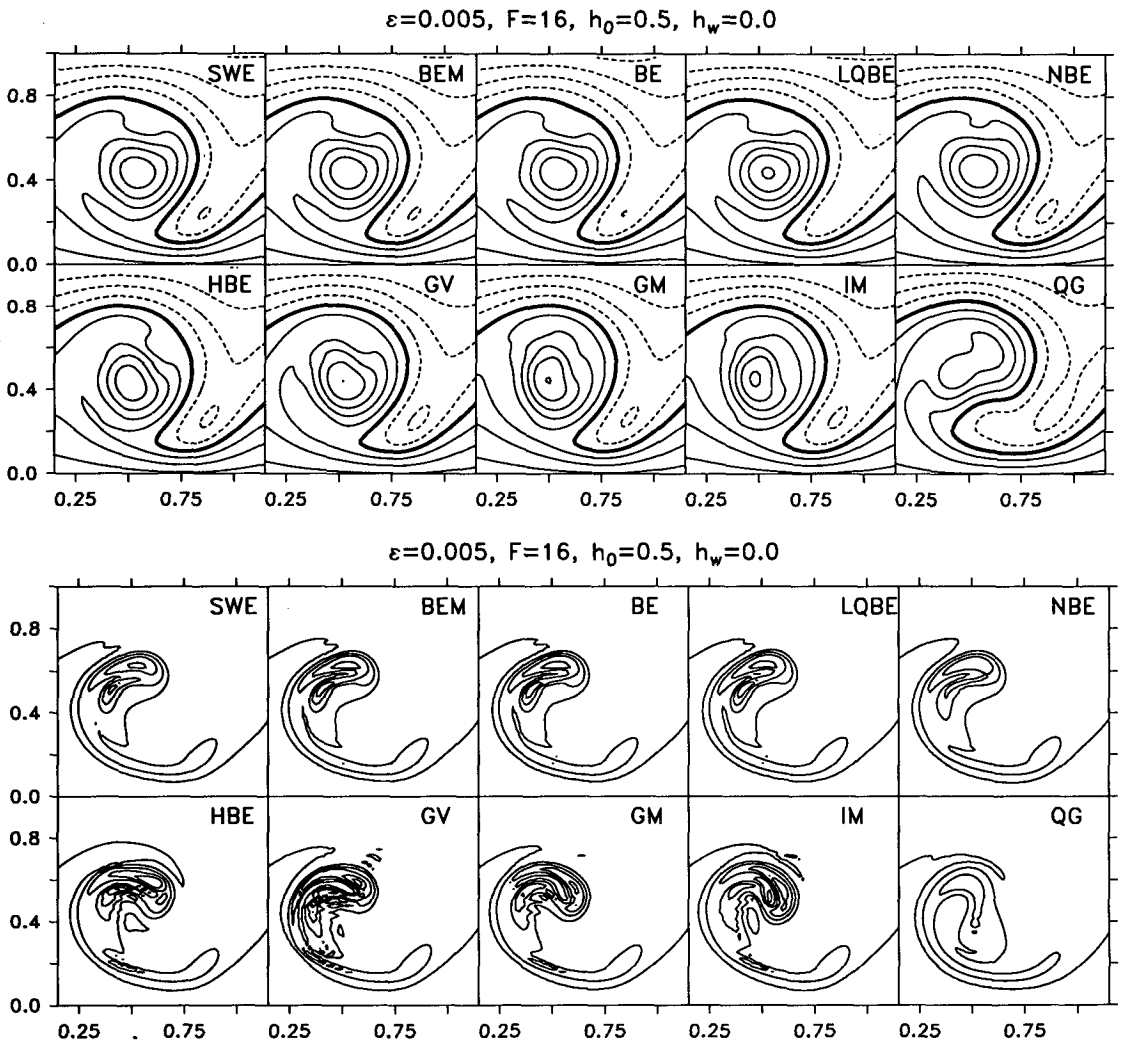

FIG. 12. Contour plots of the η (top) and potential vorticity (bottom) fields from each model, with the potential vorticity calculated as explained in the text, at $t = t_F = 0.5$ for case 2. Contour intervals are 0.1 for η and 0.2 for potential vorticity. Contour lines as in Fig. 8.

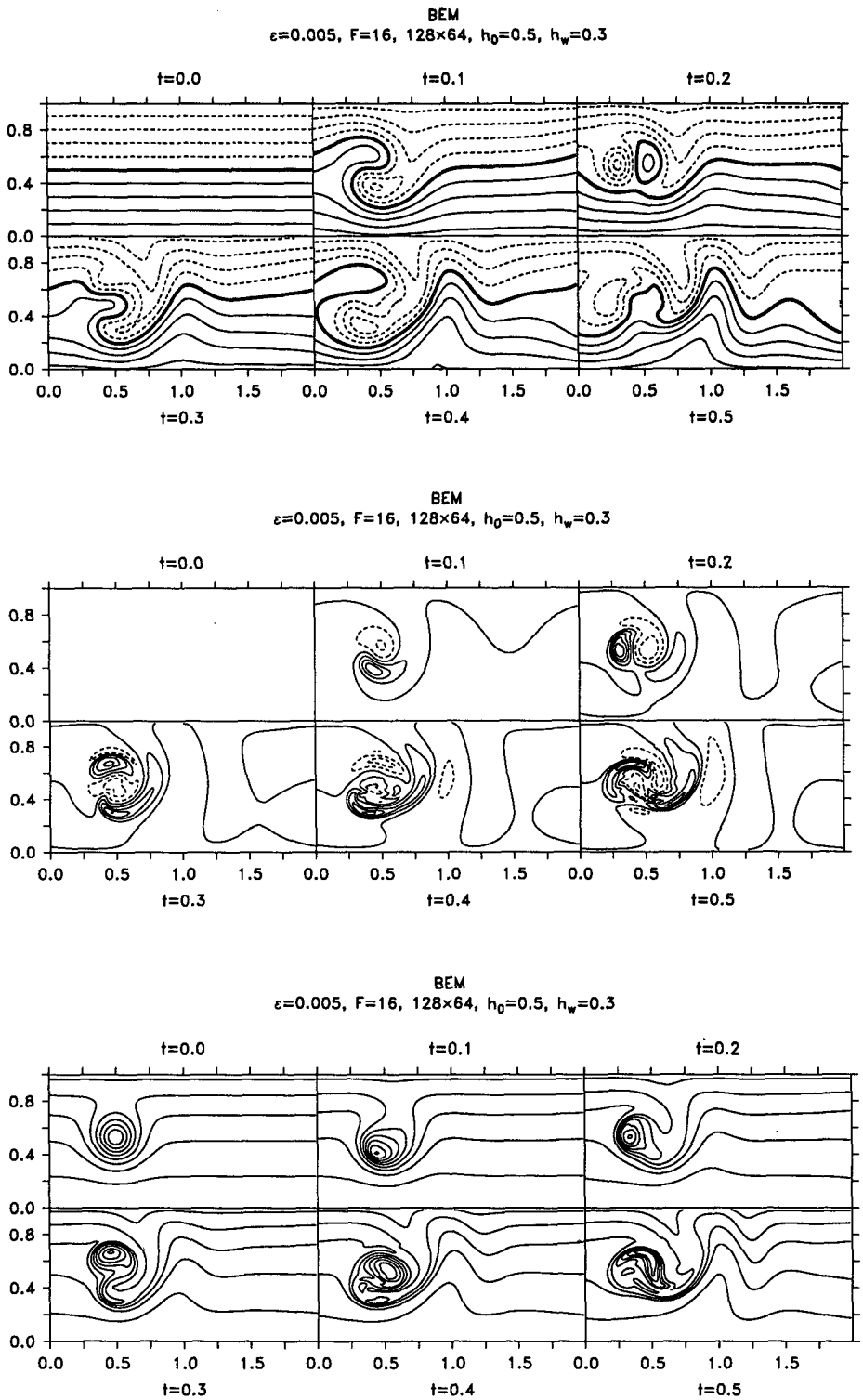

FIG. 13. Contour plots of the η (top), $\epsilon\zeta$ (middle), and Q (bottom) fields at time intervals of 0.1 from BEM for case 3. Contour intervals are 0.1 for η, 0.1 for $\epsilon\zeta$, and 0.15 for Q. The η and $\epsilon\zeta$ contour lines as in Fig. 8. The Q contour values at $x = 0$ increase from $Q = 0.85$ for increasing y.

SWE. This indicates the magnitude of the local Rossby number characterizing that particular flow. From Fig. 7, we see that for case 1, $-0.17 < \epsilon_L < 0.17$ while for case 2, $-0.37 < \epsilon_L < 0.48$, so that these cases may be characterized as low and moderate Rossby number flows, respectively. For cases 3 and 4 (not shown in Fig. 7), we find $-0.28 < \epsilon_L < 0.5$ and $-0.4 < \epsilon_L < 0.38$, respectively, so that these are also moderate Rossby number flows.

In Fig. 8 we show the time evolution of the η, ζ, and Q fields for case 1. The η and ζ fields show the initial time-dependent development of two eddies, with vorticity of opposite sign, over the bump. These eddies are subsequently stretched so that by $t = 0.08$ they have started to wrap around themselves. The Q field is a useful indicator of fluid particle motion since Q is nearly conserved (with weak friction) on fluid particles for SWE, BE, and BEM. There is evidence for some advection of Q around the top of the hill, but during this short (in terms of advection) total time period there is clearly no transport of Q off the bump. Additional calculations (not shown) out to $t = 0.18$ indicate that the fluid particles with the large Q values seem to remain trapped over the hill in a Taylor column, and show no evidence, at least to that time, of being advected off the hill.

The plot of rms error (4.18) in Fig. 9 shows that for this low Rossby number flow all of the intermediate models give reasonably accurate solutions, while QG gives an inaccurate result. Additional calculations show that as the bump height h_0 is decreased, with the other parameters fixed, QG gives increasingly better results that are similar to the other models when $h_0 = 0.1$.

The η, ζ and Q fields for case 2 are shown in Fig. 10. Again, η and ζ show the initial development of two eddies, with vorticity of opposite sign, over the hill. However, these two eddies are distorted rapidly such that by $t = 0.3$ a single time-dependent anticyclonic eddy appears to emerge and dominate the motion over the hill. The distribution with time of the Q field shows some evidence of anticyclonic advection around the hill. Advection of Q off the hill by the relatively intense positive u velocities near $y = 0$, indicated by the tightly bunched η contours there, is also clearly evident by $t = 0.4$.

To provide an additional qualitative measure of model accuracy in case 2, we plot contours of η and of the relevant measure of potential vorticity from each model at $t = 0.5$ in Fig. 12. The potential vorticity is given for the SWE by (2.7) with ζ from (2.3g), for BE, BEM, and HBE by (2.7) with ζ from (3.31), and for NBE by (2.7) with (3.59a). For LQBE, GV, and IM the potential vorticity is Q_G given by (3.12b), for GM the appropriate potential vorticity is Q_{GM} (3.19b), and for QG it is $Q_{QG} = 1 + \epsilon Q_0$, with Q_0 given by (3.3b). For SWE, we plot inertial-period-averaged values of Q.

From Fig. 12 we can see that the visual impression of the agreement between the η and Q fields of the SWE and the respective η and Q fields of the models is very similar to that provided by the quantitative error measure (4.18) plotted in Fig. 11. It is apparent from Fig. 11 that BEM and BE give the most accurate solutions, with errors of the same magnitude as those found for SW2. LQBE also does well with errors only slightly greater than BEM and BE. The other intermediate models have substantially larger errors and decrease in accuracy in the order NBE, HBE, GV, GM, and IM. The greatest error is given by QG. A striking feature of the plots of potential vorticity in Fig. 12 is the extremely close agreement of the highly-contorted Q fields of BE, BEM and LQBE with those of SWE. This good agreement is notable in the case of LQBE, since that model involves geostrophic velocities u_G and v_G in ζ_G and Q_G, whereas BE and BEM involve u_R and v_R in ζ and Q. The difference in the accuracy of LQBE and GV is readily apparent and of interest because both of these models are set up to conserve Q_G (with no friction) in different ways. For LQBE, Q_G is conserved (3.27) on particles moving with velocities ($u_G + \epsilon\chi_x$, $v_G + \epsilon\chi_y$) whereas in GV, Q_G is conserved (3.12a) on particles moving with (u, v) as given by (3.11a,b). Clearly, the LQBE method is more successful. That may be related to the fact that the vorticity ζ_G in the conserved Q_G is equal to the vorticity of the advection velocities in the Q_G equation for LQBE, but not for GV. It is worthwhile noting, as mentioned in Parts I and II, that BE and BEM are the only other intermediate models that possess that same property and that BE, BEM, and LQBE give the most accurate solutions.

Cases 3 and 4 involve the same ϵ and h_0 as in case 2, but have, in addition, uniform across-channel slopes

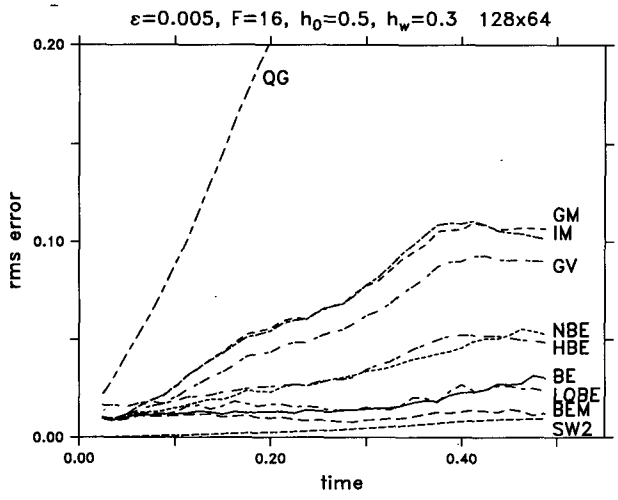

FIG. 14. The rms error (4.18) from the intermediate models, QG, and SW2 compared to SWE for case 3.

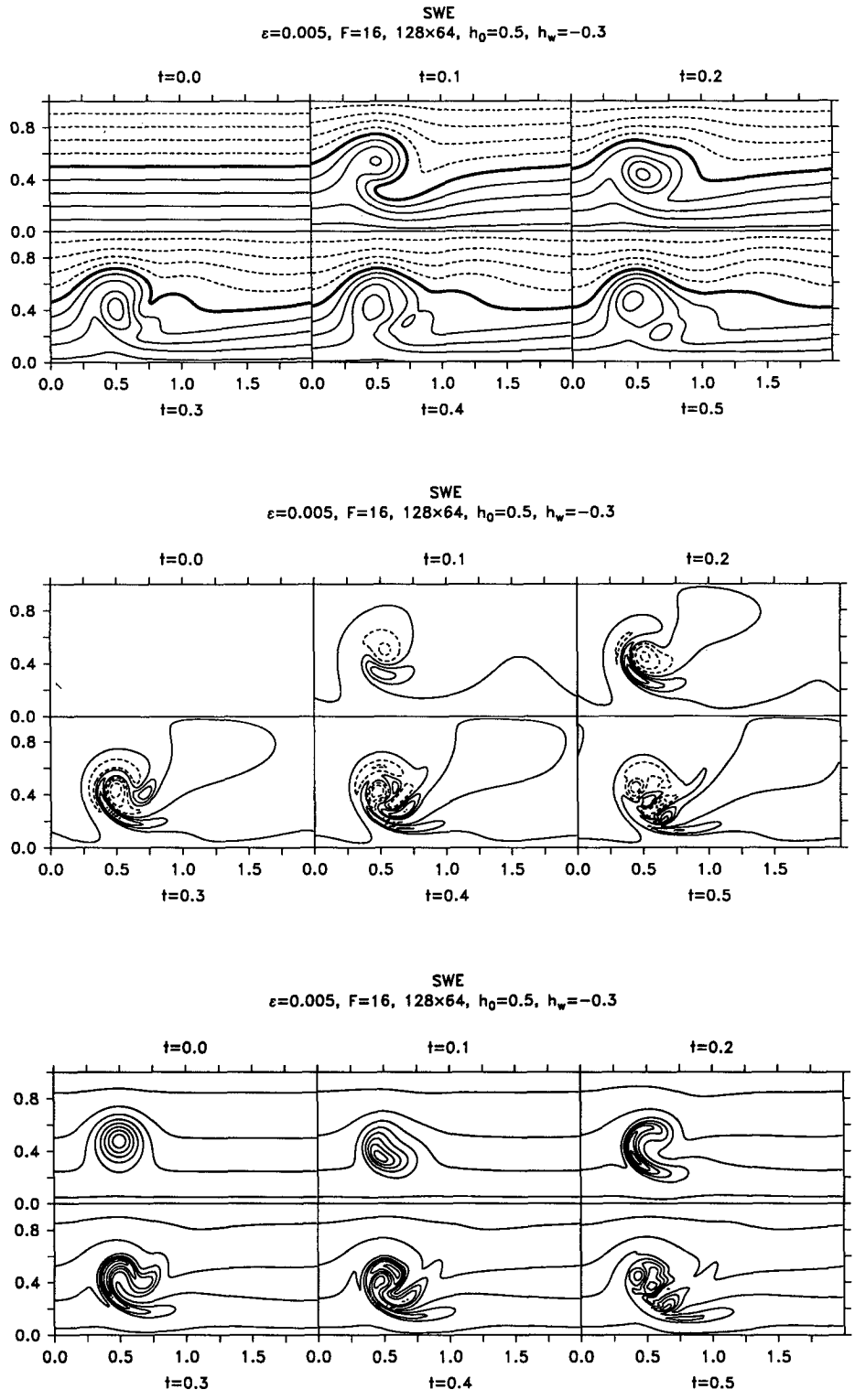

FIG. 15. Contour plots of the η (top), $\epsilon\zeta$ (middle), and Q (bottom) fields at time intervals of 0.1 from SWE for case 4. Contour intervals are 0.1 for η, 0.1 for $\epsilon\zeta$, and 0.15 for Q. The η and $\epsilon\zeta$ contour lines as in Fig. 8. The Q contour values at $x = 0$ increase from $Q = 0.85$ for decreasing y.

in the bottom topography (4.15) with $h_W = 0.3$ and $h_W = -0.3$, respectively. The linear low-frequency wave modes for constant bottom slope are discussed in section 4. The scaled wave speeds $\hat{c}_i = \epsilon c_i = \epsilon\omega_i/k$ for the first four modes with $k = \pi/4$ and $h_W = 0.3$ are given in Table 1. These values are very close to those obtained with $k = \pi/8$ and thus close to the nondispersive long wave limit. For $\epsilon = 0.005$, the magnitudes of the wave phase velocities are greater than the advection velocity ($u = 1$) for the first five modes, which are comprised of two modified Kelvin wave modes and three topographic modes. This situation, where $|c| > |u|$ for the low mode topographic waves, is similar to that for the continental shelf off the U.S. West Coast where the lowest coastally trapped wave modes have phase velocities in the long-wave limit that are larger in magnitude than typical alongshore current velocities.

In case 3, the bottom slope $h_{By} = 0.6 > 0$ and the phase velocity of the linear topographic wave modes is in a direction opposite to the initial advection velocity $u = 1$. The time development of the η, ζ, and Q fields is shown in Fig. 13. For short times $t < 0.2$, those fields evolve in a manner similar to that for case 1, but for larger times there are substantial variations. The most obvious difference involves the development here for $t > 0.2$ of standing topographic lee waves downstream of the bump. These are most visible in the ζ field where they appear to have a wavelength ≈ 0.5. This wavelength is similar to the value $2\pi(\epsilon^{-1}h_{By} - \pi^2)^{-1/2} \approx 0.6$ that is predicted by quasi-geostrophic linear theory for stationary topographic-Rossby waves in a uniform current (Pedlosky 1987, section 3.18). Relatively strong across-channel velocities are evidently associated with these lee waves and their effects may be seen in the evolution of the Q field downstream of the bump.

The plot of error measure (4.18) for case 3 (Fig. 14) is similar to case 2 and shows the same ordering. BEM, BE and LQBE give accurate solutions. The other intermediate models are less accurate with errors increasing in the order NBE, HBE, GV, GM, IM. The QG solution contains large errors.

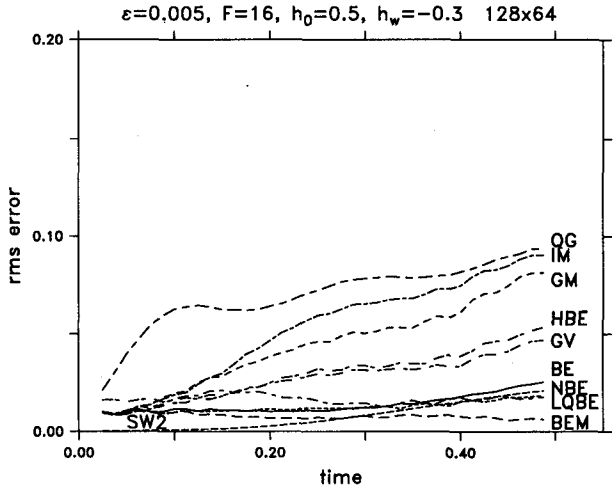

FIG. 16. The rms error (4.18) from the intermediate models, QG, and SW2 compared to SWE for case 4.

In case 4, the bottom slope $h_{By} = -0.6 < 0$ and the linear topographic wave phase velocity is in the same direction as the initial current $u = 1$. The initial evolution of the η and ζ fields (Fig. 15) is similar to case 2, but with stronger development over the bump here of the anticyclonic eddy relative to the cyclonic one. Compared with case 2, the propagation of topographic waves in the same direction as the current appears to lead to a weakening of the gradients in the η field and to a substantially attenuated vorticity field in the vicinity of the bump for $t \geq 0.4$. The errors (Fig. 16) of all models are generally smaller than in cases 2 and 3. The conclusions are similar, however. BEM gives the most accurate solutions, with BE, NBE, and LQBE having errors of only slightly larger magnitude. Again, GV, HB, GM, and IM have substantially greater errors and the QG error is largest.

We point out again that the models BEM, BE, and LQBE that give the most accurate solutions in these four cases all have analogues of potential vorticity conservation on fluid particles. In addition, we note, consistent with area integrals of their respective vorticity equations, these models have analogues [(3.55) for BEM and BE, (3.14) for LQBE] of the conservation of boundary circulation in the SWE (2.14).

6. Summary

The ability of all the intermediate models considered here to represent linear ageostrophic Kelvin and topographic wave dynamics is demonstrated by numerical solutions. The formulation of wall boundary conditions for the intermediate models and the implementation of those conditions in finite-difference form appear to be satisfactory.

The evaluation of model accuracy by comparison of numerical solutions for initial-value problems involving flow over O(1) topographic variations provides clear-cut conclusions. These are in agreement with the results from Part II. In the case 1 flow problem characterized by small values of local Rossby number, all of the intermediate models give reasonably accurate solutions while QG gives inaccurate results. For the flow problems at moderate values of local Rossby number, the performance of the different intermediate models varies considerably. BEM and BE consistently produce accurate solutions. LQBE also does well, with errors generally only slightly larger than BEM and BE. The other intermediate models have substantially less accurate solutions with errors usually increasing in the order NBE, HBE, GV, GM, and IM. In all these cases, QG produces inaccurate solutions. As was found in

Part II, BEM and BE, followed closely by LQBE, appear to be the most accurate intermediate models.

Acknowledgments. This research was supported jointly by the National Science Foundation under Grant OCE-8620403, by the Institute for Naval Oceanography under Subcontract S8765, and by the Office of Naval Research under Contract N00014-87-K-0009 (Coastal Transition Zone Program) and Contract N00014-90-J-1051. Many of the computations described here were carried out at the National Center for Atmospheric Research (project No. 35271038), which is funded by the National Science Foundation. The authors thank F. Beyer and M. Stewart for typing the manuscript.

APPENDIX A

Numerical Methods

The numerical finite-difference approximations utilized for SWE, QG and all of the intermediate models in section 3 are discussed in this appendix. To facilitate the presentation of the finite-difference equations, the operators

$$\delta_x\phi = \frac{1}{\Delta x}\left[\phi\left(x + \frac{\Delta x}{2}\right) - \phi\left(x - \frac{\Delta x}{2}\right)\right], \quad \text{(A1a)}$$

$$\bar{\phi}^x = \frac{1}{2}\left[\phi\left(x + \frac{\Delta x}{2}\right) + \phi\left(x - \frac{\Delta x}{2}\right)\right], \quad \text{(A1b)}$$

are defined for both x and y directions. Also, we use

$$\nabla^2\phi = (\delta_x^2 + \delta_y^2)\phi, \quad \bar{\phi}^{xy} = \bar{\bar{\phi}}^{xy}, \quad \text{(A1c,d)}$$

and $J(a, b)$ will denote the Arakawa formulation of the Jacobian (Arakawa 1966).

The QG and all intermediate models are formulated on a rectangular A grid (Arakawa and Lamb 1977) which has uniform grid spacing in x and in y, but allows $\Delta x \neq \Delta y$. The walls at $y = 0$, 1 are centered between grid points in y. Variables are defined along a row of grid points a distance $\Delta y/2$ outside the boundary and are calculated or specified there so that the appropriate boundary condition is satisfied. The models are time-stepped using the leapfrog–trapezoidal scheme (Kurihara 1965) for QG, IM, GV, HBE, NBE and the Adams-Bashforth scheme (Haltiner and Williams 1980) for GM, LQBE and BE. For simplicity, we will describe those models as if they were all time-differenced by the Adams-Bashforth method (or by the basic leapfrog scheme). The change to a leapfrog–trapezoidal scheme involves adding a second step, but that is straightforward. We will also use the notation $\phi^n = \phi(n\Delta t)$ to denote time level.

In the time integrations, the size of the time step for SWE and SW2 was restricted by the CFL condition (e.g., Haltiner and Williams 1980) for the Kelvin waves, i.e., by essentially

$$\Delta t \leq \Delta x/c_{KW} = \Delta x\epsilon F^{1/2}. \quad \text{(A2a)}$$

The intermediate models misrepresent the Kelvin waves (section 4) so that they become dispersive. It may be shown that for the intermediate models the stability condition for linear Kelvin waves with x-dependence (4.6) is

$$\Delta t \leq \Delta x\epsilon\left\{F + \frac{2}{\Delta x^2}[1 - \cos(k\Delta x)]\right\}^{1/2}, \quad \text{(A2b)}$$

using, e.g., the leapfrog time-difference scheme. For the Kelvin wave calculations in section 4, the Δt values for SWE and SW2 and for the intermediate models were chosen small enough to satisfy the CFL condition (A2a). For the flow problems in section 5, the intermediate models were successfully run with Δt values about 4 to 8 times as large as the limit in (A2a), evidently because any Kelvin waves produced by the topographic interactions had large enough x-wavenumbers k to give an increase in the Δt limit in (A2b) of that magnitude. The time step used for QG was generally the same as for the intermediate models.

The spatial grid size for the computations in section 5 was taken as small as possible consistent with the reasonable use of computer resources. The grid size chosen seems satisfactory based on the resolution of the vorticity and potential vorticity fields demonstrated in Figs. 8, 10, 13 and 15. From the potential vorticity fields in Fig. 12, we see that SWE and the more accurate intermediate models BE, BEM and LQBE resolve the smallest scale features in the potential vorticity better than HBE, GV, GM, and IM. The general behavior at the smallest scales would probably have been improved in all models by using regular biharmonic friction in both directions rather than (2.15). The general adequacy of grid resolution was further demonstrated by calculations with SWE, BE and QG for all the cases in section 5 with grid spacing twice as large. The resulting flow patterns for η were visually the same and the conclusions from the rms error plots were identical.

The relative computation times required by the different models on the NCAR Cray-XMP for the cases in section 5 were generally in the following ranges (expressed as a ratio to the QG time): QG 1; BE, LQBE, GV, GM, IM 5–6; SWE 8; BEM, HBE 9–10; NBE 14–15. The accurate models BE and LQBE took less computational time than SWE, but more than QG. Other intermediate models took similar or longer times than SWE. It is important to note, however, that for the intermediate models in these initial studies we have concentrated on developing stable numerical time in-

tegration schemes and have not made an extensive effort to make the models as fast as possible. It seems very likely that more efficient numerical schemes can be developed.

a. SWE

The SWE (2.1) are solved numerically by time stepping three equations for u, v and η. The finite-difference model (SWE) is implemented on a C grid (Arakawa and Lamb 1977) using the potential enstrophy conserving scheme of Arakawa and Lamb (1981). A second formulation (SW2) uses the following spatial difference scheme (Haidvogel, personal communication) which is also on a C grid:

$$\epsilon F\eta_t + \delta_x[\bar{h}^x u] + \delta_y[\bar{h}^y v] = 0, \quad \text{(A3a)}$$

$$\epsilon(\bar{h}^x u)_t + \epsilon\delta_x[h(\bar{u}^x)^2] + \epsilon\delta_y[\bar{h}^{xy}\bar{u}^y\bar{v}^x] - \overline{\bar{v}^y h}^x = -\bar{h}^x\delta_x\eta - \nu\bar{h}^x\delta_x{}^4 u, \quad \text{(A3b)}$$

$$\epsilon(\bar{h}^y v)_t + \epsilon\delta_x[\bar{h}^{xy}\bar{v}^x\bar{u}^y] + \epsilon\delta_y[h(\bar{v}^y)^2] + \overline{\bar{u}^x h}^y = -\bar{h}^y\delta_y\eta - \nu\bar{h}^y\delta_x{}^4 v. \quad \text{(A3c)}$$

The channel wall boundary conditions $v = 0$ are straightforward to implement in both C grid formulations. Both SWE and SW2 use the leapfrog–trapezoidal time-differencing scheme.

b. QG

The following equation corresponding to (3.4),

$$(\nabla^2 - F)\eta_t' = -J(\eta, \nabla^2\eta + \epsilon^{-1}h_B) - \epsilon^{-1}\nu\delta_x{}^4\nabla^2\eta, \quad \text{(A4)}$$

is solved with

$$\overline{\eta_t'}^y = 0, \quad \text{at} \quad y = 0, 1, \quad \text{(A5)}$$

where $\overline{\eta'}^y(t = 0) = 0$ on $y = 0, 1$. Additional variables η_1 and η_2, defined as the solutions to

$$(\nabla^2 - F)\eta_{1,2} = 0, \quad \text{(A6)}$$

with

$$\bar{\eta}_1^y = 0, \quad \bar{\eta}_2^y = 1, \quad \text{at} \quad y = 0, \quad \text{(A7a,b)}$$

$$\bar{\eta}_1^y = 1, \quad \bar{\eta}_2^y = 0, \quad \text{at} \quad y = 1, \quad \text{(A7c,d)}$$

are found before starting the time integration. At each time step, η'^{n+1} is obtained from $\eta_t'^n$ by the time-differencing scheme and then η^{n+1} is given by

$$\eta^{n+1} = \eta'^{n+1} + C_1{}^{n+1}\eta_1 + C_2{}^{n+1}\eta_2, \quad \text{(A8)}$$

where $C_1{}^{n+1}$ and $C_2{}^{n+1}$ are chosen so that the integral constraints (3.7a,b) are satisfied in difference form (McWilliams 1977). For the solution of (A4) with boundary condition (A5), η_t' is specified on the exterior row of grid points at $y = -\Delta y/2$ and $y = 1 + (\Delta y/2)$ so that (A5) is satisfied. In order for the Arakawa–Jacobian on the right-hand side of (A4) to give a correct zero contribution to a sum over the area ($0 \leq y \leq 1$, $0 \leq x \leq L^{(x)}$), we use the additional "computational" condition that, for the terms in $J(\eta, \Delta^2\eta + \epsilon^{-1}h_B)$,

$$\delta_y(\nabla^2\eta + \epsilon^{-1}h_B) = 0, \quad \text{at} \quad y = 0, 1. \quad \text{(A9)}$$

c. IM and GV

The formulations for IM and for GV are similar. We describe that used for GV, where (3.13) is solved with boundary conditions from (3.11a) with $v = 0$. For convenience in application of the channel wall boundary conditions, the right-hand side of (3.13a) is kept in the divergence form it originally takes following derivation from the substitution of (3.11a,b) in the continuity equation (2.1a). In difference form (3.13a) is

$$\delta_x(\bar{h}_G^y\delta_x\eta_t) + \delta_y(\bar{h}_G^y\delta_y\eta_t) - F\eta_t = -\epsilon^{-1}\delta_x(\bar{h}_G^x\delta_y\overline{\mathcal{B}_G}^{xy}) + \epsilon^{-1}\delta_y(\bar{h}_G^y\delta_x\overline{\mathcal{B}_G}^{xy}) - \epsilon^{-1}\nu\delta_x(\bar{h}_G^x\delta_x{}^4 v_G) + \epsilon^{-1}\nu\delta_y(\bar{h}_G^y\delta_x{}^4 u_G), \quad \text{(A10)}$$

with boundary conditions,

$$\delta_y\eta_t = \epsilon^{-1}\delta_x\overline{\mathcal{B}_G}^{xy} + \epsilon^{-1}\nu\delta_x{}^4 u_G, \quad \text{at} \quad y = 0, 1, \quad \text{(A11)}$$

where

$$v_G = \delta_x\eta, \quad u_G = -\delta_y\eta. \quad \text{(A12a,b)}$$

We solve (A10) for η_t by utilizing the fast Poisson solver described in Part II, which is modified here to use a Fourier transform in x and tridiagonal matrix inversion in y. (For the wave calculations in section 4 where $\Delta x = 2\Delta y$ a sparse matrix solver was used in place of the fast Poisson solver for GV, IM, GM, HBE and NBE.) The time-differencing scheme then gives η^{n+1}. For the application of boundary condition (A11), the term $\delta_x(\overline{\delta_y\eta)^2}^y/2$ in $\epsilon^{-1}\delta_x\overline{\mathcal{B}_G}^{xy}$ requires a value of η along a row of exterior grid points a distance $3\Delta y/2$ outside the boundaries. For the values of η at these grid points, which are needed only in this term, we use extrapolation, e.g., for (A11) at $y = 0$,

$$\eta(-3\Delta y/2) = 3\eta(-\Delta y/2) - 3\eta(\Delta y/2) + \eta(3\Delta y/2). \quad \text{(A13)}$$

d. GM

For GM, (3.20a) is solved with boundary conditions from (3.16b) with $v = 0$. As for GV and IM, (3.20a) is written in divergence form. The resulting finite-difference equation from (3.20a) is

$$\delta_x[\bar{h}_{GM}^x(1 + \epsilon\delta_y\overline{u_G}^{xy})\delta_x\eta_t] + \delta_y[\bar{h}_{GM}^y(1 + \epsilon\delta_x\overline{v_G}^{xy})\delta_y\eta_t]$$

$$- F\eta_t = \epsilon\delta_x[\bar{h}^x_{GM}(\overline{\delta_y v_g}^{\,y})\delta_y\bar{\eta}_t^{\,xy}] + \epsilon\delta_y[\bar{h}^y_{GM}(\overline{\delta_x u_G}^{\,x})\delta_x\bar{\eta}_t^{\,yx}] - \epsilon^{-1}\delta_x(\bar{h}^x_{GM}\delta_y\overline{\mathcal{B}_G}^{\,xy}) + \epsilon^{-1}\delta_y(\bar{h}^y_{GM}\delta_x\overline{\mathcal{B}_G}^{\,yx}) - \epsilon^{-1}\nu\delta_x[\bar{h}^x_{GM}\delta_x{}^4 v_G) + \epsilon^{-1}\nu\delta_y(\bar{h}^y_{GM}\delta_x{}^4 u_G), \quad \text{(A14)}$$

with boundary conditions

$$(1 + \epsilon\delta_x\bar{v}^y_G)\delta_y\eta_t = \epsilon(\overline{\delta_x u_G}^{\,x})\delta_x\bar{\eta}_t^{\,yx} + \epsilon^{-1}\delta_x\overline{\mathcal{B}_G}^{\,xy} + \epsilon^{-1}\nu\delta_x{}^4 u_G, \quad \text{at} \quad y = 0, 1. \quad \text{(A15)}$$

We solve (A14) for η_t with (A15) by using the fast Poisson solver described in Part II. The time-differencing scheme then gives η^{n+1}.

e. NBE and HBE

The formulations for NBE and HBE are similar. We describe that used for NBE, where (3.61) and (3.60) are solved with boundary conditions for (3.61) from (3.57a) with $v = 0$ and for (3.60) from (3.48). We drop the subscript 0 on ψ_0, h_{R0}, and $\mathcal{B}_{R0}$, and let

$$\eta = \psi + \epsilon\eta'. \quad \text{(A16)}$$

Again for convenience in application of boundary conditions, (3.61) and (3.60) are written in divergence form. With (A16), the finite-difference form of (3.61) is

$$\delta_x(\bar{h}^x_R\delta_x\psi_t) + \delta_y(\bar{h}^y_R\delta_y\psi_t) - F\psi_t = \epsilon F\eta'_t - \epsilon^{-1}\delta_x(\bar{h}^x_R\delta_y\overline{\mathcal{B}_R}^{\,xy}) + \epsilon^{-1}\delta_y(\bar{h}^y_R\delta_x\overline{\mathcal{B}_R}^{\,yx}) - \epsilon^{-1}\nu\delta_x(\bar{h}^x_R\delta_x{}^4 v_R) + \epsilon^{-1}\nu\delta_y(\bar{h}^y_R\delta_x{}^4 u_R), \quad \text{(A17)}$$

with boundary conditions, from (3.57a) with $v = 0$, of

$$\delta_y\psi_t = \epsilon^{-1}\delta_x\overline{\mathcal{B}_R}^{\,xy} + \epsilon^{-1}\nu\delta_x{}^4 u_R, \quad \text{at} \quad y = 0, 1, \quad \text{(A18)}$$

where

$$v_R = \delta_x\psi, \quad u_R = -\delta_y\psi. \quad \text{(A19a,b)}$$

The finite difference form of (3.60) is

$$\nabla^2\eta' = -\delta_x[\overline{u_R}^{\,xy}\delta_x\overline{u_R}^{\,y} + v_R\overline{\delta_y u_R}^{\,x}] - \delta_y[u_R\overline{\delta_x v_R}^{\,y} + \overline{v_R}^{\,xy}\delta_y\overline{v_R}^{\,x}], \quad \text{(A20)}$$

with boundary condition from (3.48) of

$$\delta_y\eta' = -[u_R\overline{\delta_x v_R}^{\,xy} + \overline{v_R}^{\,xy}\delta_y\overline{v_R}^{\,x}], \quad \text{at} \quad y = 0, 1. \quad \text{(A21)}$$

To solve (A17) and (A20) an iteration procedure is utilized. With ψ^n and η'^n and values at earlier time steps known, estimate $\eta'^n_t = (\eta'^n - \eta'^{n-1})/\Delta t$. Use this estimate in (A17). Solve (A17) with (A18) for ψ_t^n in the same manner as described for η_t in (A10). Obtain an estimate for ψ^{n+1} from ψ_t^n using the time-differencing scheme. Substitute this in the right-hand side of (A20) and solve (A20) for η'^{n+1}. This gives a new estimate for η'^n_t from an inversion of the time-difference scheme. This value of η'^n_t is substituted in (A17) and the cycle is repeated until convergence for ψ^{n+1} and η'^{n+1} is obtained.

f. BE

The governing equations are (3.52), (3.34) and (3.50). We use the definition (A16) so that in difference form (3.52) and (3.50) are

$$(\nabla^2 - F)\psi_t = \epsilon F\eta'_t - J(\psi, \zeta - \tilde{H}) - \epsilon\delta_x[\overline{(\zeta - \tilde{H})}^{\,x}\delta_x\chi] - \epsilon\delta_y[\overline{(\zeta - \tilde{H})}^{\,y}\delta_y\chi] - \epsilon^{-1}\nu\delta_x{}^4\nabla^2\psi, \quad \text{(A22)}$$

$$\nabla^2\chi = -J(\psi, \zeta) - \epsilon\delta_x[\bar{\zeta}^x\delta_x\chi] - \epsilon\delta_y[\bar{\zeta}^y\delta_y\chi] - \epsilon^{-1}\nu\delta_x{}^4\nabla^2\psi - \nabla^2\psi_t, \quad \text{(A23)}$$

where

$$\zeta = (\delta_x{}^2 + \delta_y{}^2)\psi = \nabla^2\psi,$$
$$\tilde{H} = \tilde{H}/\epsilon = F\eta - \epsilon^{-1}h_B. \quad \text{(A24a,b)}$$

The finite-difference form of (3.34), with definition (A19), is (A20). A boundary condition on $\delta_y\psi_t$ for (A22) is obtained from (A18). The boundary condition

$$v = \overline{\delta_x\bar{\psi}^{\,y}}^{\,x} + \epsilon\delta_y\chi = 0 \quad \text{at} \quad y = 0, 1. \quad \text{(A25)}$$

along with the additional "computational" conditions,

$$\delta_y\zeta = 0, \quad \delta_y\tilde{H} = 0 \quad \text{at} \quad y = 0, 1, \quad \text{(A26a,b)}$$

are utilized for the terms on the right-hand side of (A22). The additional conditions (A26a,b) are similar to (A9) for QG and are used so that the area sum of the Arakawa–Jacobian term $J(\psi, \zeta - \tilde{H})$ and the divergence terms involving χ are correctly equal to zero when (A25) holds. For (A23), we apply boundary conditions (A18), (A25), and (A26a). The boundary condition for (A20) is (A21).

The equations (A22), (A20), and (A23) are solved by iteration. With ψ^n, η'^n, χ^{n-1}, ψ_t^{n-1}, η_t^{n-1} assumed known, use extrapolation to estimate $\eta'^n_t = 2\eta'^{n-1}_t - \eta'^{n-2}_t$, $\chi^n = 2\chi^{n-1} - \chi^{n-2}$. Use these estimates in (A22) and solve (A22) for ψ_t^n. Find ψ^{n+1} from ψ_t^n and the time-difference scheme. Use ψ^{n+1} and $\nabla^2\psi_t^n$ in (A20) and (A23). Solve (A20) for η'^{n+1} and find η'^n_t from η'^{n+1} and inversion of the time-difference scheme. Solve (A23) for χ^n. Return to the step where (A22) is solved for ψ_t^n and repeat the cycle until convergence for χ^n, ψ_t^n, and η'^n_t is obtained. Finally, find ψ^{n+1} and η'^{n+1} from ψ_t^n and η'^n_t, respectively, with the time-difference scheme.

g. BEM

The governing equations for BEM are (3.52), (3.51) and (3.50). These are the same as for BE, with the

exception that (3.51) in BEM replaces (3.34) in BE. Thus, in difference form we have (A22) and (A23), with the same boundary conditions (A18), (A25), and (A26) as used for BE. The finite-difference form of (3.51), with definitions (A16) and (A19), is

$$\nabla^2\eta' = -\delta_x[\overline{u_R}^{xy}\delta_x\overline{u_R}^{y} + v_R\overline{\delta_y u_R}^{x} - \epsilon\overline{\zeta\overline{\delta_y\chi}^{y}}^{x}]$$
$$- \delta_y[u_R\overline{\delta_x v_R}^{y} + \overline{v_R}^{xy}\delta_y\overline{v_R}^{x} + \epsilon\overline{\zeta\overline{\delta_x\chi}^{x}}^{y}], \quad \text{(A27)}$$

with boundary condition from (3.54),

$$\delta_y\eta' = -[u_R\overline{\delta_x v_R}^{y} + \overline{v_R}^{xy}\delta_y\overline{v_R}^{x} + \epsilon\overline{\zeta\overline{\delta_x\chi}^{x}}^{y}],$$
$$\text{at} \quad y = 0, 1. \quad \text{(A28)}$$

The presence of χ in (A27) makes the solution procedure outlined above for BE inappropriate, since χ is needed at the same time levels as ψ and η (see the discussion in Appendix B). Therefore, we use a different iteration scheme where ψ^n, η'^n, χ^n, ψ_t^n, $\eta_t'^n$ are assumed to be known and iteration of (A22), (A23) and (A27) is used to provide new values for all of these variables at the next time step $(n+1)$. This iteration procedure is similar to that developed for BE by Norton et al. (1986) for application to (3.50), (3.34) and an omega equation to find χ (Parts I and II). In this case, estimate $\psi^{n+1} = \psi^{n-1} + 2\Delta t\psi_t^n$, $\eta'^{n+1} = \eta'^{n-1} + 2\Delta t\eta_t'^n$, $\chi^{n+1} = 2\chi^n - \chi^{n-1}$, $\eta_t'^{n+1} = 2\eta_t'^n - \eta_t'^{n-1}$. Use these estimates in (A22) and solve (A22) for ψ_t^{n+1}. Correct $\psi^{n+1} = \psi^n + \Delta t(\psi_t^{n+1} + \psi_t^n)/2$. Calculate χ^{n+1} from (A23). Use this value of χ^{n+1} in (A27) and calculate η'^{n+1} from (A27). Find $\eta_t'^{n+1} = 2(\eta'^{n+1} - \eta'^n)/\Delta t - \eta_t'^n$. Finally, use $\eta_t'^{n+1}$, ψ^{n+1}, χ^{n+1} in (A22) and solve (A22) for ψ_t^{n+1}. Return to the step where ψ^{n+1} is corrected and repeat the cycle until convergence for ψ^{n+1}, η'^{n+1}, χ^{n+1}, ψ_t^{n+1}, and $\eta_t'^{n+1}$ is obtained. This method may also be used for BE.

h. LQBE

The governing equations for LQBE, (3.28) and (3.26), are the same as (2.1a) and (3.50) for BE and BEM with $\psi = \eta$. Thus, for LQBE we may use the same formulation given for BE with the simplification that $\eta' = 0$ and the balance equation (A20) is omitted. Alternately, we may use the formulation for BEM with $\eta' = 0$ and with (A27) omitted. We choose the latter alternative for the solutions presented here.

APPENDIX B

BEM Model

The BEM model (section 3g), based on the continuity equation (2.1a) and the momentum equations (3.49a,b) and governed by (3.50), (3.51) and (3.52), has an additional complicating feature that was not explicitly addressed in Parts I and II. The presence of χ in the balance equation (3.51) leads to the possibility of spurious time-dependent solutions and requires additional considerations for the specification of initial values. For BE, the time derivative of the balance equation (3.34) involves ψ_t and η_t and may be used consistently with the equations for η_t (2.1a) and for $\nabla^2\psi_t$ (3.50) in the solution procedure. For BEM, the time derivative of (3.51) involves ψ_t, η_t, and χ_t, while no other equation for χ_t exists. The implications of this are most easily seen in the linear β-plane problem, where similar behavior occurs, and it is worthwhile to examine the equations in that case.

The linear BEM continuity and momentum equations on a flat-bottom β-plane where the dimensionless Coriolis parameter is

$$f = 1 + \epsilon\beta y, \quad \text{(B1)}$$

are

$$F\eta_t + \nabla^2\chi = 0, \quad \text{(B2a)}$$
$$\epsilon u_{Rt} - fv = -\eta_x, \quad \text{(B2b)}$$
$$\epsilon v_{Rt} + fu = -\eta_y. \quad \text{(B2c)}$$

The vorticity and divergence equations that follow from (B2b,c) are

$$\zeta_t + \beta v + f\nabla^2\chi = 0, \quad \text{(B2d)}$$
$$f\nabla^2\psi = \nabla^2\eta + \epsilon\beta u_R + \epsilon^2\beta\chi_x, \quad \text{(B2e)}$$

so that (B2a,d,e) may be considered the governing equations. Note that the $\epsilon^2\beta\chi_x$ term in (B2e) is identical in form to a term that would appear in the nonlinear f-plane BEM divergence equation (3.51) in the presence of a vorticity field if $\zeta = \beta y$. The omega equation for (B2), obtained by substituting ∇^2 (B2a), (B2b), and (B2d) in the time derivative of (B2a), is

$$\nabla^4\chi - Ff^2\nabla^2\chi - \beta F(2fv - \eta_x) = \epsilon^2\beta F\chi_{xt}. \quad \text{(B3)}$$

The equations (B2a,d,e) are similar to the linear "modified balance equations" considered by Moura (1976) and to the linearized global balance equations (gBE) discussed by Gent and McWilliams (1983b). Relevant linear wave solutions for those models were discussed in Moura (1976) and Gent and McWilliams (1983b) and both analyses showed the existence of spurious, high-frequency time-dependent solutions.

The nature of the solutions to (B2a,d,e) may be assessed by examining modulated wave solutions for $\epsilon \ll 1$ with a slowly varying Coriolis parameter f (B1) (e.g., Grimshaw and Allen 1988). The results show that modulated waves exist with approximate dispersion relations,

$$\omega = -\beta k/(K^2 + f^2F) \quad \text{(B4a)}$$

and

$$\omega = \frac{(K^2 + F)K^2}{\epsilon^2\beta kF}, \quad \text{(B4b)},$$

where ω is the frequency, (k, l) are the wavenumbers in the (x, y) directions, and $K^2 = k^2 + l^2$. The frequency (B4a) corresponds to the expected Rossby wave solution where $O(\eta/\chi) = O(\psi/\chi) = O(1)$. In the Rossby wave, the balance in (B2d) involves all three terms and the primary balance in (B3) is between the terms on the left-hand side. The second frequency (B4b), where $\omega = O(\epsilon^{-2})$, corresponds to the spurious high-frequency oscillation found in Moura (1976) and Gent and McWilliams (1983b). For this wave, $O(\eta/\chi) = O(\psi/\chi) = O(\epsilon^2)$ and the primary balance in (B2d) is between ζ_t and $f\nabla^2\chi$. In (B3), the approximate balance is between the three terms involving χ and this leads directly to the approximate dispersion relation (B4b). In addition, if we consider the governing equations to be (B2d,e) and (B3), we see that initial values for both $\psi(t = 0)$ and $\chi(t = 0)$ may be specified. This differs from BE, where the $\epsilon^2\beta\chi_x$ and $\epsilon^2\beta F\chi_{xt}$ terms are absent from (B2c) and (B3), respectively. In BE, only the initial value of $\psi(t = 0)$ is specified and $\eta(t = 0)$ and $\chi(t = 0)$ are then determined by the BE forms of (B2e) and (B3). To reduce initial excitation of the spurious high-frequency oscillation in BEM, it appears from (B2) and (B3) that BEM should be initialized by specifying $\psi(t = 0)$, similar to BE, and by determining $\eta(t = 0)$ and $\chi(t = 0)$ such that (B2e) and (B3) are satisfied with $\chi_{xt}(t = 0) = 0$ in (B3).

Behavior related to that found above for BEM in the linear β-plane problem, involving the possibility of spurious high-frequency oscillations and initial-value requirements, may be expected to occur for BEM in the nonlinear f-plane problem in the presence of nonzero vorticity fields. The situation is more complicated in that case, however, because χ enters (3.51) through the nonlinear term $\epsilon^2 J(\zeta, \chi)$. In obtaining numerical solutions to the BEM model, the method of initialization of the fields and the choice of finite-difference time integration scheme must evidently be utilized to filter out effects of the spurious high-frequency waves. The initialization can be accomplished, using the above considerations of the linear β-plane problem as a guide, by the specification of $\psi(t = 0)$ only, as in BE, and the subsequent determination of $\eta(t = 0)$ and $\chi(t = 0)$ using the equations (3.50), (3.51) and (3.52) and an assumed additional initial condition of $\chi_t(t = 0) = 0$. Following the initialization of the fields, the variables may be stepped forward in time using the procedure discussed in Appendix A. Based on the high accuracy of the BEM solutions found in sections 4 and 5 and in Part II, it appears that this method has been effective in the cases studied.

REFERENCES

Allen, J. S., J. A. Barth and P. A. Newberger, 1990: On intermediate models for barotropic continental shelf and slope flow fields: Part I, Formulation and comparison of exact solutions. *J. Phys. Oceanogr.*, **20,** 1017–1042.

Arakawa, A., 1966: Computational design for long-term numerical integrations of the equations of atmospheric motion. *J. Comput. Phys.*, **1,** 119–143.

——, and V. R. Lamb, 1977: Computational design of the basic dynamical processes of the UCLA general circulation model. *Methods of Computational Physics,* J. Chang, Ed., Vol. 17, Academic Press, 173–265.

——, and ——, 1981: A potential enstrophy and energy conserving scheme for the shallow-water equations. *Mon. Wea. Rev.*, **109,** 18–36.

Barth, J. A., J. S. Allen and P. A. Newberger, 1990. On intermediate models for barotropic continental shelf and slope flow fields: Part II, Comparison of numerical model solutions in doubly periodic domains. *J. Phys. Oceanogr.*, **20,** 1044–1076.

Ball, F. K., 1965: The effect of rotation on the simpler modes of motion of a liquid in an elliptic paraboloid. *J. Fluid Mech.*, **22,** 529–545.

Bolin, B., 1955: Numerical forecasting with the barotropic model. *Tellus,* **7,** 27–49.

——, 1956: An improved barotropic model and some aspects of using the balance equations for three-dimensional flow. *Tellus,* **8,** 61–75.

Charney, J. G., 1955: The use of primitive equations of motion in numerical prediction. *Tellus,* **7,** 22–26.

——, 1962: Integration of the primitive and the balance equations. *Proc. Int. Symp. Numerical Weather Prediction,* Tokyo, Meteor. Soc. Japan, 131–152.

Cushman-Roisin, B., W. H. Heil and D. Nof, 1985: Oscillations and rotations of elliptic warm-core rings. *J. Geophys. Res.*, **40,** 11 756–11 764.

Gent, P. R., and J. C. McWilliams, 1983a: Consistent balanced models in bounded and periodic domains. *Dyn. Atmos. Oceans,* **7,** 67–93.

——, and ——, 1983b: The equatorial waves of balanced models. *J. Phys. Oceanogr.*, **13,** 1179–1192.

——, and ——, 1984: Balanced models in isentropic coordinates and the shallow-water equations. *Tellus,* **36A,** 166–171.

Grimshaw, R., and J. S. Allen, 1988: Low-frequency baroclinic waves off coastal boundaries. *J. Phys. Oceanogr.*, **18,** 1124–1143.

Haidvogel, D. B., and K. H. Brink, 1986: Mean currents driven by topographic drag over the continental shelf and slope. *J. Phys. Oceanogr.*, **16,** 2159–2171.

Haltiner, G. J., and R. T. Williams, 1980: *Numerical Prediction and Dynamic Meteorology.* 2nd ed. Wiley, 477 pp.

Hoskins, B. J., 1975: The geostrophic momentum approximation and the semi-geostrophic equations. *J. Atmos. Sci.*, **32,** 233–242.

——, 1982: The mathematical theory of frontogenesis. *Ann. Rev. Fluid Mech.*, **14,** 131–151.

Kurihara, Y., 1965: On the use of implicit and iterative methods for the time integration of the wave equation. *Mon. Wea. Rev.*, **93,** 33–46.

Lorenz, E. N., 1960: Energy and numerical weather prediction. *Tellus,* **12,** 364–373.

McWilliams, J. C., 1977: A note on a consistent quasi-geostrophic model in a multiply connected domain. *Dyn. Atmos. Oceans,* **1,** 427–441.

——, and P. R. Gent, 1980: Intermediate models of planetary circulations in the atmosphere and ocean. *J. Atmos. Sci.*, **37,** 1657–1678.

Moura, A. D., 1976: The eigensolutions of the linearized balance equations over a sphere. *J. Atmos. Sci.*, **33,** 877–907.

Norton, N. J., J. C. McWilliams and P. R. Gent, 1986: A numerical model of the balance equations in a periodic domain and an example of balanced turbulence. *J. Comput. Phys.*, **67,** 439–471.

Pedlosky, J., 1987: *Geophysical Fluid Dynamics.* Springer-Verlag, 710 pp.